

Multimegawatt DAE δ ALUS Cyclotrons for Neutrino Physics

M. Abs^j, A. Adelman^{b,*}, J.R. Alonso^c, W.A. Barletta^c, R. Barlow^h, L. Calabretta^f, A. Calanna^c, D. Campo^c, L. Celona^f, J.M. Conrad^c, S. Gammino^f, W. Kleeven^j, T. Koeth^a, M. Maggiore^e, H. Okuno^g, L.A.C. Piazza^e, M. Seidel^b, M. H. Shaevitz^d, L. Stingelin^b, J. J. Yang^c, J. Yeckⁱ

^a*Institute for Research in Electronics and Applied Physics, University of Maryland, College Park, Maryland, 20742*

^b*Paul Scherrer Institut, CH-5232 Villigen, Switzerland*

^c*Department of Physics, Massachusetts Institute of Technology*

^d*Columbia University*

^e*Istituto Nazionale di Fisica Nucleare - LNL*

^f*Istituto Nazionale di Fisica Nucleare - LNS*

^g*RIKEN, Nishina Center for Accelerator-Based Science, Hirosawa, Wako 351-0198, Japan*

^h*Huddersfield University, Queensgate Campus, Huddersfield, HD1 3DH, UK*

ⁱ*IceCube Research Center, University of Wisconsin, Madison, Wisconsin 53706*

^j*IBA-Research*

Abstract

DAE δ ALUS (Decay-At-rest Experiment for δ_{CP} studies At the Laboratory for Underground Science) provides a new approach to the search for CP violation in the neutrino sector. High-power continuous-wave proton cyclotrons efficiently provide the necessary proton beams with an energy of up to 800 MeV to create neutrinos from pion and muon decay-at-rest. The experiment searches for $\bar{\nu}_\mu \rightarrow \bar{\nu}_e$ at short baselines corresponding to the atmospheric Δm^2 region. The $\bar{\nu}_e$ will be detected via inverse beta decay. Thus, the cyclotrons will be employed at a future ultra-large gadolinium-doped water or scintillator detector.

In this paper we address the most challenging questions regarding a cyclotron-based high-power proton driver in the megawatt range with a kinetic energy of 800 MeV. Aspects of important subsystems like the ion source and injection chain, the magnet design and radio frequency system will be addressed.

Precise beam dynamics simulations, including space charge and the H₂⁺ stripping process, are the base for the characterization and quantification of the beam halo—one of the most limiting processes in high-power particle accelerators.

Keywords: High-Power Cyclotron, Conceptual Design, Space charge

1. Introduction

The DAE δ ALUS Collaboration is designing advanced cyclotrons that accelerate molecular hydrogen ions to produce decay-at-rest neutrino beams in a novel search for CP violation in the neutrino sector. The required cyclotrons must exceed the performance of the world's current best-performing cyclotron, at the Paul Scherrer Institut (PSI), in both energy and power, while, at the same time, maintaining cost-effectiveness.

*Corresponding author

Email addresses: michel.abs@iba-group.com (M. Abs), andreas.adelmann@psi.ch (A. Adelman), jralonso@lbl.gov (J.R. Alonso), barletta@mit.edu (W.A. Barletta), R.Barlow@hud.ac.uk (R. Barlow), calabretta@lns.infn.it (L. Calabretta), alessandra.calanna@gmail.com (A. Calanna), dcampo@lns.infn.it (D. Campo), celona@lns.infn.it (L. Celona), conrad@MIT.EDU (J.M. Conrad), gammino@lns.infn.it (S. Gammino), Willem.Kleeven@iba-group.com (W. Kleeven), koeth@umd.edu (T. Koeth), mario.maggiore@lnl.infn.it (M. Maggiore), okuno@riken.jp (H. Okuno), piazza@lns.infn.it (L.A.C. Piazza), mike.seidel@psi.ch (M. Seidel), shaevitz@nevis.columbia.edu (M. H. Shaevitz), Lukas.Stingelin@psi.ch (L. Stingelin), Jianjun.Yang@psi.ch (J. J. Yang), jim.yeck@icecube.wisc.edu (J. Yeck)

We begin by discussing the experimental context for the machines, providing the requirements which constrain the design described in this paper. The next section addresses the options for ions accelerated, leading to the identification of H_2^+ as the most promising candidate. Subsequent sections address individual subsystems of the accelerator complex, giving performance requirements and our design concept for meeting these requirements. Designs are generally based on existing accelerator facilities, so necessary extrapolations are anchored on demonstrated performance. Areas are identified where technical innovations might possess elevated risks, and programs are described to reduce or mitigate these risks.

This paper addresses only the accelerator systems necessary to produce the beams of the required power and energy; the high-power target/dump systems required for pion production are recognized as requiring substantial physics and engineering design, and will be addressed in subsequent studies. A cyclotron-based system is studied here, as we are convinced that the compactness and most probably substantially lower cost of cyclotrons (over linacs) are telling advantages.

1.1. Goals of the project

The physics community has placed the search for evidence for CP violation in the neutrino sector at the highest priority [50–52]. CP Violation in the light neutrino sector would manifest as a difference in the oscillation probability for neutrinos versus antineutrinos. This is a key piece of evidence for the theory of leptogenesis [53, 54]. The search is also motivated by the experimental observation of CP violation in quarks. Why would the quark sector show CP violation if the lepton sector does not? What would this say about quark-lepton unification?

The goal of the DAE δ ALUS experiment is the search for a nonzero CP violation parameter, δ . The signal is observed in $\bar{\nu}_\mu \rightarrow \bar{\nu}_e$ oscillations. The flux is provided by 800 MeV protons impinging on a carbon target producing pions from the Δ resonance. These come to rest in the target and subsequently decay via the chain: $\pi^+ \rightarrow \nu_\mu \mu^+$ followed by $\mu^+ \rightarrow e^+ \bar{\nu}_\mu \nu_e$. The resulting $\bar{\nu}_\mu$ flux is peaked and cuts off at 52.8 MeV as shown in Fig. 1. It is isotropic with a well-known energy dependence for each of the three flavors, driven

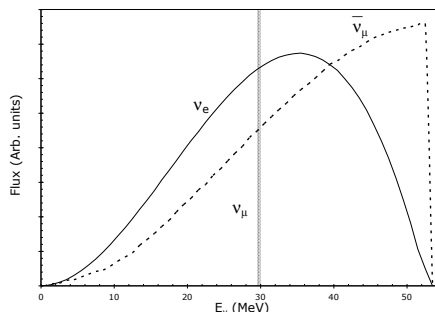


Figure 1: The energy distribution for a decay-at-rest flux.

by the weak interaction. Because almost all π^- capture before decay, the $\bar{\nu}_e$ fraction in the beam is expected to be $\sim 4 \times 10^{-4}$ of the other neutrino flavors.

This CP violation signal is extracted by measuring the oscillation wave as a function of distance (L) the neutrinos have travelled, as illustrated in Fig. 2. The DAE δ ALUS design calls for measurements at three values: $L = 1.5$ km, 8 km, and 20 km. Three accelerator complexes, called “near, mid, and far site,” are used, with the neutrinos impinging on a single ultra-large detector, which may contain gadolinium-doped water or scintillator. In order to connect the events to the accelerator site where the neutrinos were produced, the sources must be run in alternating time intervals. Also, roughly 50% of the run must be accelerator-off to allow measurement of beam-off backgrounds in the detector. DAE δ ALUS requires average powers of 0.8, 1.6, and 4.8 MW from each site. The duty factors and the instantaneous power may be varied to achieve this.

The average power of each station was chosen such that DAE δ ALUS matches the sensitivity of the 2011 design of the Long Baseline Neutrino Experiment (LBNE), a conventional neutrino beam experiment, to CP violation [7]. However, neutrino beams of this type suffer from high systematic errors in this search. The DAE δ ALUS multi cyclotron design offers a statistics-limited alternative approach. When DAE δ ALUS data is combined with the conventional beam data in neutrino mode, the result is better than the expectation of a conventional beam with an intensity upgrade, like Project-X [55]. Thus, this project has a very high discovery potential and is an exciting option for the particle physics community.

1.2. Layout of the proposed facility and basic parameters

The DAE δ ALUS three-accelerator-station design [55] is illustrated in Fig. 2. The near station measures the initial flux, the mid station is at half of oscillation maximum, and the far station is at oscillation maximum. Thus the oscillation wave can be traced as a function of L/E (E denoting the energy of the beam), allowing sensitivity to δ , as is illustrated in Fig. 2.

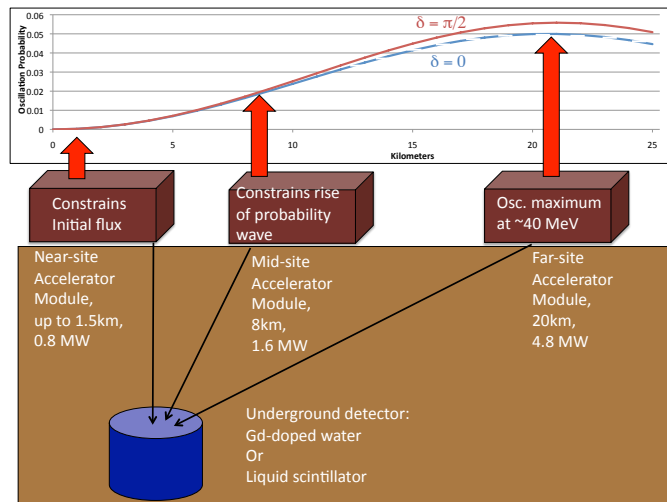


Figure 2: Schematic of the layout of DAE δ ALUS accelerator modules. The powers at the respective modules, are average values based on a 20% duty cycle.

The simplest and least expensive option is to construct identical accelerator units — “modules” — which can be run for different time periods or grouped to provide the required power at each station. Hence we focus here on the design of a single accelerator module.

A module consists of four basic components: the ion source (IS) and low-energy beam transport (LEBT); the Injector Cyclotron (DIC); and the DAE δ ALUS Superconducting Ring Cyclotron (DSRC). Each module will also have its own dedicated target/dump, which must all be identical to ensure commonality of the neutrino sources.

As will be shown in section 2, we have selected H_2^+ as the ion to be accelerated. The DIC accelerates the beam to 60 MeV/amu, and extracts it with a “classical” electrostatic septum system. The H_2^+ beam is transported to the DSRC, injected, and accelerated to the top energy of 800 MeV/amu. A foil stripper converts the H_2^+ into two protons that follow an extraction trajectory and are removed cleanly from the accelerator for transport to the target/dump.

The 800 MeV/amu energy is selected to be comfortably above the pion production threshold, enabling good thick-target yields of π^+ , but low enough to minimize contaminating π^- production and decay in flight of the negative pions, an undesirable background.

1.3. Possible connections with research beyond neutrino physics

The two accelerators, DIC and DSRC, that form the basis of a module, have applications beyond this experiment, such as in industry.

1.3.1. Medical isotope production

The DAE δ ALUS Injector Cyclotron can accelerate more than 5 mA of particles with charge-to-mass ratio of 1-to-2, including H_2^+ and α -particles, up to 60 MeV/amu. This is in the energy range commonly used for medical isotope facilities. Isotopes that are produced at these energies which are useful to the medical industry include ^{52}Fe , ^{122}Xe , ^{28}Mg , ^{128}Ba , ^{97}Ru , ^{117}Sn , and ^{82}Sr [44].

Cyclotrons on the market from IBA Cyclotron Solutions [74] and BEST Cyclotrons [75] produce $\lesssim 1$ mA of protons at 70 MeV. At the China Institute of Atomic Energy (CIAE), a compact 100 MeV H^- cyclotron is being assembled, designed for currents up to 500 μA [76]. Other designs have been studied for delivery of 2 mA of 70 MeV protons [44]. Our DIC will produce 5 mA of H_2^+ , which is equivalent of 10 mA of protons — a significant increase in the beam current.

1.3.2. Subcritical reactors

The DIC-DSRC combination is a promising source for accelerator-driven systems (ADS) [56, 57]. They provide an attractive approach to treatment of waste from reactors by burning and transmutation long-lived isotopes to shorter-lived ones, significantly easing the long-term storage requirements for this waste. Recent studies from the Nuclear Energy Agency (NEA) and the Organisation for Economic Co-operation and Development (OECD) [58, 59] detail these possibilities. Specifically, heavy transuranic elements with half-lives of many tens of thousands of years can be transmuted to lighter isotopes with half-lives of 1000 years or less. In fact, the DAE δ ALUS H_2^+ concept originated from a cyclotron for ADS development [60, 61].

Another angle of application is that of a subcritical core of fissile materials. Such a core, having a K factor less than 1, will be inherently “safe” from a criticality accident. Such a core may consist of material such as thorium which cannot be configured with a K greater than 1. However, in principle, a proton beam of sufficient energy and power could provide a neutron flux adequate to drive K to 1 for such structures thus producing a “fail-safe” reactor because as soon as the beam goes away, the K drops below 1. The power available from such a reactor depends on the proton power provided and the K factor without beam, so for instance a $K = 0.95$ would provide a multiplication factor of 20, and a $K = 0.98$, a factor of 50. A 10 MW beam into a $K = 0.98$ core could produce a reactor yielding 500 MW. This would be more than adequate to provide the power to drive the accelerator system, and deliver substantial power to the grid [43]. It is important to deliver the beam power relatively uniformly over the volume of the core, and a proton energy of 800 – 1000 MeV would adequately bathe a core of several cubic meters with secondary neutrons.

1.4. Phasing of DAE δ ALUS: science of the sub-projects

The DAE δ ALUS project is being developed in phases that allow establishment of the viability of each stage of the system. Phase 1, development and testing of the ion source, is underway, as described in this paper. Phase 2 involves a full-scale test of the DIC and associated LEBT. This opens interesting scientific opportunities that are now under study, as discussed here. Phase 3 is the construction of the first full accelerator module, which opens a “near and mid site accelerator” physics program, also discussed below. Phase 4 is the full three-site plan for the CP violation search described above. In this section we focus on the physics case for Phases 2 and 3.

1.4.1. An Isotope Decay-at-Rest (isoDAR) beam produced using the DIC

The injector provides a current of 5 mA H_2^+ at 60 MeV. As discussed above, this has applications in medical isotope production. Here we consider its application to discovery science, as a driver for an isotope decay-at-rest (IsoDAR) electron antineutrino source. The design uses the protons from the DIC to generate a high neutron flux which impinges on ^7Li , with 99.99% isotopic purity, to produce ^8Li , which subsequently decays. When paired with an existing scintillator-based detector (approximately 1 kton), this $\langle E_\nu \rangle = 6.4$ MeV source produces inverse beta decay (IBD) interactions ($\bar{\nu}_e + p \rightarrow e^+ + n$) as well as $\bar{\nu}_e$ -electron scatters.

A wide range of physics studies are possible with this intense, flavor-pure source. Ref. [73] describes the unprecedented sensitivity to electron antineutrino disappearance at $\Delta m^2 \sim 1 \text{ eV}^2$, reaching $> 10\sigma$ and including the capability to distinguish between one and two sterile neutrinos models. The source also provides a unique ultra-large sample of $\bar{\nu}_e$ -electron scatters for Beyond Standard Model tests. Also, one can search for new particles produced in the target that electromagnetically decay in the detector.

1.4.2. Physics from a first “near accelerator”

The first stand-alone accelerator module can produce a decay-at-rest beam from stopped pions and muons for a unique short-baseline neutrino program, exploiting the well-defined flux of $\bar{\nu}_\mu$, ν_μ and ν_e . This module is likely to be the “Near Accelerator” for the CP violation studies, and hence will be placed near an ultra-large gadolinium-doped water detector or a scintillator detector. At the same time, it is likely to be in a location where additional smaller detectors can be installed underground nearby. The physics program of the “Near Accelerator” can exploit both arrangements. Here we provide two examples.

Ref. [62] describes how this source can be paired with an experiment like LENA [72] to study the signal for $\bar{\nu}_\mu \rightarrow \bar{\nu}_e$ and ν_e disappearance at high Δm^2 . This study is complementary to IsoDAR, which searches for $\bar{\nu}_e$ disappearance, allowing for interesting tests of models of multiple sterile neutrinos, including those with CP and CPT (Charge, Parity, and Time Reversal) violations. For the appearance channel, pairing with a LENA-like detector, provides a stringent test of the LSND and MiniBooNE signal regions at $> 5\sigma$ and of $\nu_e > 3\sigma$.

A proposal for a small, dedicated short-baseline experiment for the purpose of discovery of coherent neutrino scattering [63] is also being considered for the “Near Accelerator”. This would be located in an underground chamber near to the module. Coherent elastic neutrino- and WIMP-nucleus (Weakly Interacting Massive Particles) interaction signatures are expected to be quite similar, and so a next-generation ton-scale dark matter detector could discover neutrino-nucleus coherent scattering, a precisely predicted Standard Model process. The flux from the decay-at-rest beam was shown to be ideal when paired with planned dark matter detectors for this search. An extension of this concept is to measure active-to-sterile neutrino oscillations with neutral current coherent neutrino-nucleus scattering [77]. The design uses multiple decay-at-rest targets, at different positions, driven by a single DAE δ ALUS accelerator to produce a neutrino flux that impinges on a single, stationary dark matter detector. This induces coherent neutrino scatters. Deviation from the expected L dependence for the events would indicate Beyond Standard Model physics.

2. H₂⁺ for the DAE δ ALUS project

Obvious choices of ion species, to obtain high-power proton beams, are bare protons, H^- , or H_2^+ . In our case, H^- can be excluded because of Lorentz stripping at the upper energies in the very strong magnetic field required for a compact machine. For example, the TRIUMF top energy is 500 MeV, and the highest field in the 18-meter diameter cyclotron is only 0.5 T. At 800 MeV, the peak field would need to be no more than 0.3 T, making for an impossibly large machine.

Protons and H_2^+ are both suitable candidates; in Table 1 key differences are identified, and a degree of risk is given with respect to the desired performance parameters. The prime advantages of H_2^+ are reduced space-charge effects at low energies (due to the presence of two protons for every charge) and the ability to extract the beam at high energy with a stripping foil, reducing the need for the clean separation between turns that is mandatory for bare protons.

The space charge of the particle beam produces a repulsive force inside the beam, which generates detuning effects. A measure of the strength of this effect, the so-called generalized perveance is defined by

$$K = \frac{qI}{2\pi\epsilon_0 m\gamma^3\beta^3}, \quad (1)$$

where q, I, m, γ and β are respectively the charge, current, rest mass and the relativistic parameters of the particle beam [69]. The higher the value of K , the stronger the space-charge detuning effects.

According to Eq. (1), the space-charge effects for the 5 mA of H_2^+ beam in the DSRC are equivalent to a 2.5 mA proton beam with the same γ . Consequently, they are similar to the space-charge effects present in

the 2.4 mA proton beam being accelerated currently at PSI. We also note that the 5 mA H_2^+ injected into the DIC has a similar K value as commercially available cyclotrons used for the production of radioisotopes. Another degree of freedom, in order to reduce space-charge effects, is of course the energy, in particular the injection energy and acceleration voltage. In this specific situation, we increase the typical injection energy of the DIC from 30 keV to 70 keV.

However, since there are many other factors, such as the external focusing and total number of turns in the cyclotrons, which have important impacts on the overall space-charge effects, we cannot get a clear picture without precise beam dynamics calculations. In this paper, the space-charge effects are studied quantitatively by self-consistent 3D models implemented in the code Object Oriented Parallel Accelerator Library (OPAL) [49]. The beam dynamics model is described in detail in [46, 47]. For the DSRC, we implemented a simple stripper model into OPAL in order to study the complex extraction trajectories of the stripped protons.

We have identified the main challenges of accelerating H_2^+ : the requirement for a substantially larger machine due to the higher magnetic rigidity of the ions, the need for a higher vacuum due to the greater probability of collisional dissociation of the ions with residual gas atoms (at least an order of magnitude better vacuum than required for protons), and the presence of loosely bound vibrational states in the H_2^+ ions emerging from the ion source.

2.1. H_2^+ Dissociation

The creation of H_2^+ ions in the ion source results in the population of vibrational states. As shown in Fig. 4, the 17 bound vibrational states have binding energies from 2.7 eV (ground state) to essentially zero. Because of molecular symmetry (implying lack of dipole coupling), the lifetime of these states is long compared to the residence time of the ion in the accelerator. The bound states result from different equilibrium distances for the protons bound by only one electron compared with two for the neutral molecule. Figure 2.1.2 shows the Franck-Condon population distribution of these states, which is roughly independent of the source environment, e.g., plasma temperature [42]. States whose binding energy is less than about 1 eV are likely to be Lorentz stripped in the 6T DSRC field at an extraction energy of 800 MeV/n; this fact is shown in Fig. 4. These ions contribute to beam loss. As the total population of states of $n = 7$ or higher is roughly 10%, the beam loss from this mechanism would be unacceptably high: 100 kW for 1 MW of extracted beam, which is a factor of 500 over the 200 watt “loss budget” [40].

Initial experiments at the vibrational state detector of Oak Ridge National Laboratory (ORNL) are ongoing, and will characterize vibrational state populations from a representative ion source, and study in a separate ion trap the collisional dissociation process of H_2^+ ions in helium gas. This will be followed by later runs testing admixtures of noble gases in the ion source itself, and optimizing the source type and geometry to produce adequate currents of H_2^+ devoid of the damaging vibrational states.

2.1.1. Cross section of H_2^+ dissociation

Survival rates of H_2^+ in C-foil were measured as functions of the foil thickness at 160 MeV/amu [5] and at 9.6 MeV/amu [4]. Cross sections of H_2^+ dissociation to two protons and an electron can be inferred from the measurements to be 8.7×10^{-19} cm² at 160 MeV/amu and 1.2×10^{-17} cm² at 9.6 MeV/amu assuming that the channel to $H^+ + H^0$ is negligible. The cross sections can be extrapolated to be 4.3×10^{-19} cm² and 2.3×10^{-19} cm² respectively at 800 MeV/amu using scaling law by $\log(E)/E$ as shown in Fig. 5. The two values at 800 MeV/amu suggest that survival rate at 800 MeV/amu on a carbon foil with a thickness of 2 mg/cm² is less than 1.0×10^{-10} . We conclude that 2 mg/cm² is thick enough to dissociate all the H_2^+ beam at the foil.

The emission of H^0 after the foil is a possible point of concern because it will be an origin of uncontrolled beam loss. The break-up rate of the H_2^+ molecule into a proton and a neutral hydrogen is considered to be small. However, we have to take into account the recombination H^+ after the H_2^+ dissociation to neutral H^0 at the foil. Following [3], the capture cross section of H^+ in the carbon foil is estimated to be 9.4×10^{-34} cm². There is clear evidence that only a small amount of H^0 will survive; however, a dedicated experiment to measure the rate of H^0 is being planned.

Table 1: Comparison of Protons vs. H_2^+ as candidates for DAE δ ALUS cyclotron beams

Requirements	Protons	H_2^+
Ion source: Current (>40 mA) Emittance ($\epsilon_n < 0.3 \pi$ mm mrad)	Demonstrated	Expected to be achievable
Ion source: species purity	Analyzer separates species other than protons	Analyzer separates species other than H_2^+
Ion Source: Control of internal degrees of freedom	Not applicable	Need to suppress higher vibrational states of H_2^+ ; requires demonstration
Injector Cyclotron (DIC): capture of adequate beam	High space charge is a challenging problem in compact cyclotrons: good capture efficiency demonstrated in separated-sector machines (PSI Injector)	Will present similar challenges, but lower perveance implies a simpler problem
DIC: Extraction	Expected to be achievable	Expected to be achievable
Ring Cyclotron (DSRC): Injection	Expected to be achievable	Expected to be achievable
DSRC: Beam rigidity	$K = 800$ Could use normal magnets	$K = 3200$ Requires large, high-field Superconducting magnets
DSRC: Beam dynamics	Resonances may limit achievable current	Dangerous resonances appear to be avoidable
DSRC: Extraction	Requires clean turn separation at high energy, very difficult to achieve	Stripping extraction with foil does not need clean turn separation, but requires control of halo in the extraction channel
DSRC: rf	Need very high-power rf to get high energy-gain/turn to obtain clean turn separation	Relatively straightforward No need for very high power
DSRC: Vacuum	Requirements easily achieved ($< 10^{-7}$ torr)	Requirements substantially more stringent ($< 10^{-8}$ torr) to minimize beam loss through gas collisions
DSRC: Beam loss concerns	Turn separation at extraction	Lorentz dissociation of unquenched vibrational states Collisions with residual gas Neutrals emerging from foil

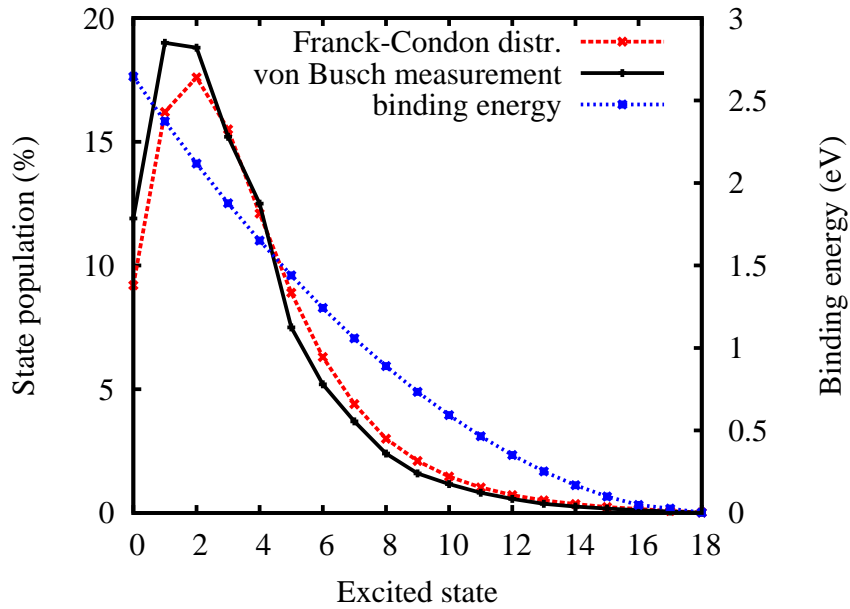


Figure 3: Vibrational state binding energies and populations for H_2^+ ions

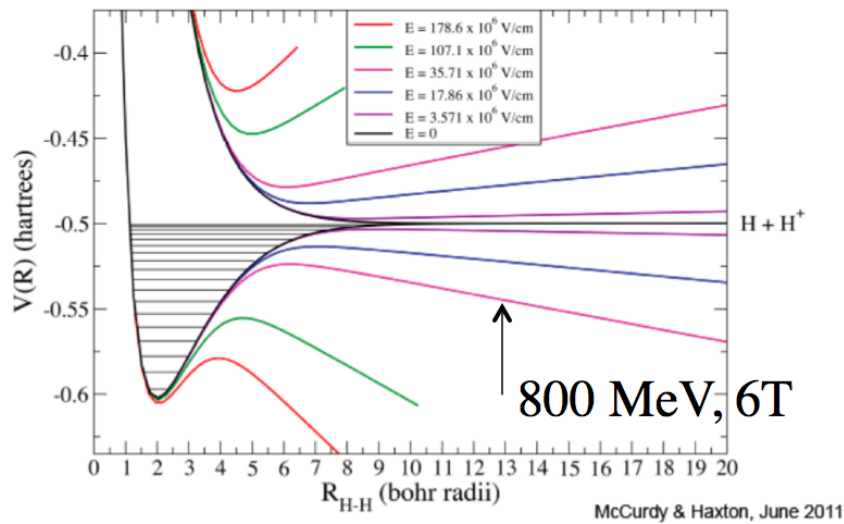


Figure 4: The H_2^+ potential well, with vibrational states are indicated by horizontal lines. Distortion of the H_2^+ potential well for an 800 MeV/amu ion in an electric field. The distorted well results in shifted levels, however these are not shown. The relativistic transformation of an 800 MeV/amu H_2^+ in a 6 T magnetic field, resulting in an apparent electric field, yields the distorted well shown in magenta, and noted with the arrow.

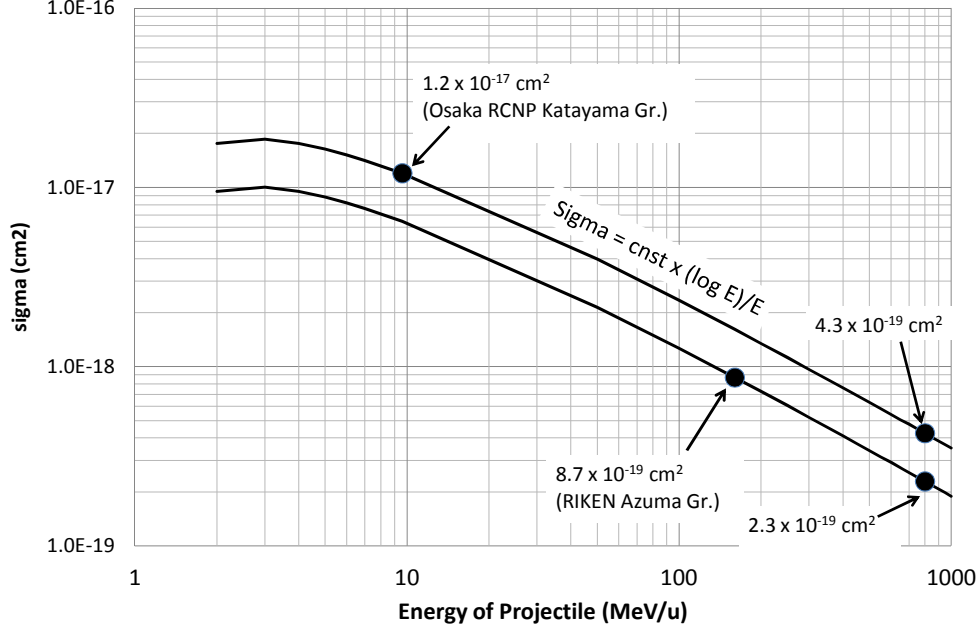


Figure 5: Energy dependence of the cross section of H_2^+ dissociation

2.1.2. Vibrational state analysis

H_2^+ ions emerging from a normal ion source will populate a range of vibrational states [6]. A technique for quenching loosely bound vibrational states has been suggested by Sen et al. [39]. This technique introduces noble gases He or Ne into the ion source because the collisional recombination reaction



is exothermic for vibrational states with a quantum number higher than three. It remains to be determined whether this mechanism can clean the beam emerging from the source of loosely bound states to better than the one part in 500 required to prevent the unacceptable beam losses, while still maintaining the high currents necessary to achieve the beam-power goals of the accelerator complex.

An experimental apparatus at ORNL, initially developed at CRYRING in Stockholm [1, 2], allows us to characterize vibrational state populations of low-energy molecular beams such as H_2^+ [37, 38]. This detector bends the H_2^+ ions through 90° into the path of a 1 nm laser beam, with an overlap of about 18 cm length. A few ions will be dissociated into a proton and a neutral hydrogen atom. The beam, largely unaffected, is bent through another 90° into a Faraday cup, but the few neutrals created will propagate through a thin foil, freeing electrons that are accelerated into a channel-plate detector for counting. While difficult to calibrate, this detection scheme is suitable for establishing the presence or absence of states with binding energies less than about 1 eV. Changing the wavelength of the laser light can probe down to different binding energies. Assuming the raw beam extracted from a typical source follows the Franck-Condon distribution shown in , the ratio of neutrals counted to Faraday cup reading should correspond, for a 1 nm laser, to about 10% of the beam.

The test stand also contains a stage where ions are slowed down and captured in a radio-frequency quadrupole (RFQ) trap, and can slowly drift through before being re-accelerated to enter the above-mentioned detector. This trap can be filled with low-pressure gas, the primary purpose of which is to cool heavier-ion products. The residency of ions in the trap is about a millisecond, substantially longer than the sub-microsecond transit time. This system was developed for use with the Holifield Radioactive Beam Facility, but can be applied for the present studies by observing whether the vibrational states can be collisionally dissociated with an appropriate gas admixture. This would be observed by a decrease in the neutral to Faraday-cup ratio in the detector. Studying this ratio as a function of gas pressure and species is expected to provide insight into the collisional dissociation process in an environment independent from the very complex conditions present in an ion source plasma.

Results from the RFQ trap experiments will lead to testing of gas mixtures in the ion source plasma, and eventually to design of the appropriate source with the long confinement times required to achieve the 500-to-1 suppression of vibrational states. A substantial R&D program is envisioned to achieve this performance. This experiment will lead to the specification and design for the DIC source capable of delivering the required very high current of H_2^+ ions free of vibrational states.

3. Ion source and Low-Energy Beam Transfer (LEBT)

The ion source for DAE δ ALUS is required to produce beams of H_2^+ ions, free of weakly bound vibrational states, and an emittance suitable for axial injection into the DIC. For the near & mid sites, the beam current out of the source must be sufficient to produce the 2 mA average proton current at 800 MeV (assuming a 20% duty factor).

To determine the required (H_2^+) current from the source, one must assess the overall efficiency of the transport and acceleration of the beam. By far the greatest losses occur during inflection and capture in the DIC. Once captured, the efficiency for transfer, acceleration, and extraction must be close to 100%.

A practical value for the phase acceptance is $\pm 10^\circ$; hence, only approximately 5% efficiency can be expected. A longitudinal bunching system in the LEBT improves the capture efficiency. Assuming a conservative bunching factor of two, an overall injection efficiency of 10% is conceivable; hence, the source has to deliver an average H_2^+ current of 50 mA. The source can be pulsed to accommodate the 20% duty factor. For optimizing the rf-system, the pulse length will be between 1 and 10 milliseconds, this leads to a reduction of the heat load on the source, allowing for higher instantaneous power, and therefore, higher beam currents.

In principle, obtaining H_2^+ ions is an easy extrapolation from conventional proton sources. An analysis of beams from such a proton source will always contain fractions of H_2^+ , H_3^+ , and other positive molecular ions arising from contaminants in the source. By adjusting operating parameters, the fraction of H_2^+ can be improved; efficiencies as high as 80% for H_2^+ have been reported [20]. However, no characterization of the vibrational state populations has been performed, nor attempts made so far to suppress the weakly bound ones.

3.1. Central region test

An experiment is being designed to study the beam dynamics from the existing Versatile Ion Source (VIS), designed and build at INFN-LNS (Catania), up to the matching point of the spiral inflector. The aim of the test is to study inflection and capture efficiency of high-current H_2^+ beams in the central region.

Figure 6 shows the beam envelope through the LEBT: a 40 cm long solenoid that focuses the beam through a collimator placed about one meter away, downstream of the Wien filter. The Wien filter will be 15 cm long, with magnets producing a field of about 850 Gauss, and a crossed electric field of about 2 kV/cm separating the components of the beam: consequently only $Q/A = 1/2$ ions have the correct velocity to pass through the filter undeflected.

At the location of the slits, 40 cm downstream, the proton and H_2^+ peaks are separated by about 6 cm. Downstream of the selection box, two quadrupoles and a second solenoid provide the necessary matching to the central region of the test cyclotron. In the actual DIC, these elements will be located within the axial

injection line. The use of skew quadrupoles will add an additional degree of freedom for matching the beam into the inflector channel.

An rf-buncher, operating at the fundamental frequency, provides longitudinal compression and, hence, better capture efficiency. Space-charge forces will limit the effectiveness of this bunching, but the lower perveance of the H_2^+ ion (compared to protons of the same velocity) is expected to be an advantage.

While the operating parameters of this test (source extraction voltage, buncher and filter parameters, and inflector design) are not likely to be exactly those of the final design for the central region of the DIC, information gained from the tests is expected to provide baseline data that can be used to benchmark simulation codes that will be used to design the actual central region.

3.1.1. The versatile ion source

The compact VIS source [29–31] is an off-resonance microwave discharge source operating at 2.45 GHz using permanent magnets and a simplified extraction geometry. Extraction from the VIS source is accomplished with a four-electrode accel-decel configuration to control backstreaming of electrons and maintain high-brightness optics for currents up to about 40 mA of protons at maximal 80 kV. The source has already demonstrated good continuous wave (CW) proton currents (>35 mA) with normalized emittance below 0.2π mm-mrad.

A preliminary test for extracting H_2^+ ions from this source yielded 20 mA from an 8 mm extraction aperture. Substantially higher currents can be obtained by increasing this aperture to 10 or 12 mm, while still maintaining an overall emittance within the expected acceptance of the cyclotron. In addition, different methods for exciting the plasma are being explored that might increase plasma density and improve source performance.

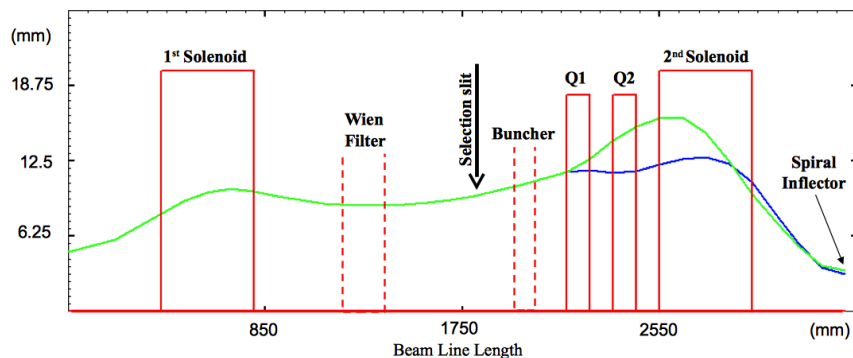


Figure 6: Beam envelope of the H_2^+ beam along the injection line, from the ion source up to the spiral inflector of the DIC

3.1.2. Bunching

The ion source delivers a beam that is continuous, on the scale of the cyclotron rf-frequency. However, the cyclotron will only accept particles arriving within a narrow phase window of $\pm 10^\circ$. This implies that only about 5% of the beam from the source will be captured in the cyclotron. In the first phase of the project a buncher in fundamental mode, and later a buncher running at the third harmonic of the rf, is expected to improve the bunching capture efficiency by factors of two to three. For bunching related discussions in this paper we assume a conservative bunching factor of two.

4. The DAE δ ALUS injector cyclotron

We study intensities between 1 and 5 mA of H_2^+ up to the energy of 60 MeV/amu, but we are deferring the discussion of the spiral inflector and the central region to a follow-up paper. A compact four-sector

cyclotron is proposed and sketched in Fig. 7. It is based on the parameters achieved by existing commercial compact machines [25] and accelerators for research purposes. Existing commercial H^- cyclotrons use axial injection of the beam at 30 keV and can accelerate and extract beam currents of about 2 mA. In this design, the H_2^+ beam is injected at about 35 keV/amu such that the generalized perveance is in the same range as for commercial cyclotrons. In this way, it is considered that the space-charge problems at injection will be equivalent to those of the proven commercial cyclotrons. However, space-charge effects at low energy and the optimization of the extraction system remain the primary challenges; they are addressed in this section.

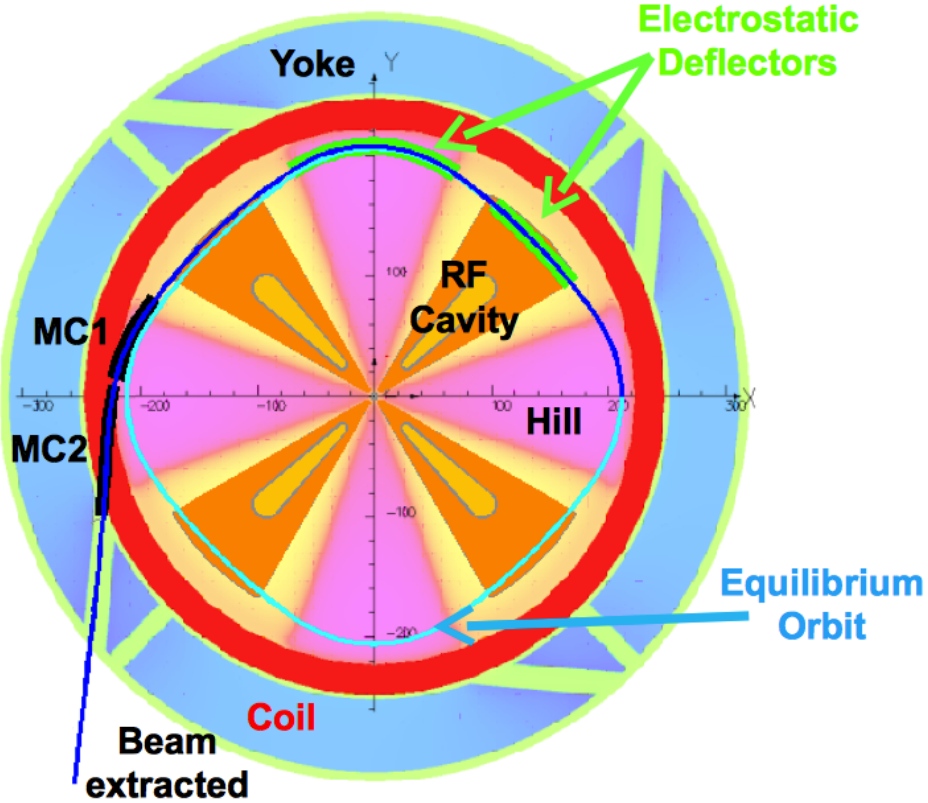


Figure 7: Layout of the DIC, a four-sector cyclotron with a pair of room temperature coils. The acceleration system consists of four rf-cavities that work at the frequency of 49.2 MHz at the 6th harmonic. The beam is injected into the center of the machine by using a spiral inflector, the extraction system includes two electrostatic deflectors and two magnetic channels. The extraction path of the H_2^+ ions are shown, starting from the 0° azimuth.

The magnetic field design has to satisfy requirements concerning beam dynamics, as well as the technical and economical feasibility of the machine. These requirements can be listed, as follows:

- minimize the effects on the beam quality due to the resonance crossing and, in particular, to guarantee the conditions of vertical and radial stability ($\nu_r > 1$ and $\nu_z > 0.5$)
- the average magnetic field errors must be on the order of a few times 10^{-4} to ensure that the integrated rf-phase slip remains smaller than 20°
- minimize the coil current density in order to reduce the power consumption and the heating of the pole

- minimize the iron weight to reduce the cost, while an acceptable value of the stray field has to be less than 500 gauss at one meter away from the cyclotron iron yoke.

A large hill gap of 10 cm was chosen to have enough space for the beam transport and to achieve a good conductance for the vacuum system. A total of eight cryopanel are located inside the dee electrode of the rf-cavities. The vacuum system will be able to achieve better than 10^{-7} mbar, which is a necessary condition to reduce the beam losses due to H_2^+ stripping.

The angular width of the hill, in the range of $28^\circ - 40^\circ$, optimizes magnetic field properties, resulting in a valley larger than 45° , allowing easily the installation of rf-cavities working at the 6th harmonic. According to our preliminary model simulation, in the acceleration region, from 0.5 to 60 MeV/amu, the isochronism accuracy is better than 5×10^{-4} . The betatron tunes are shown in Fig. 8. The H_2^+ reaches 61.7 MeV/amu after 107 turns, maintaining an integrated phase shift in a narrow range of about $\pm 10^\circ$ (excluding the extraction region), as is shown in Fig. 9.

Results from OPAL simulations show that space charge helps to form an approximately circular and stationary beam distribution in the horizontal-longitudinal plane. However, a beam halo on the order of 10^{-4} of the intensity is formed. In order to reduce the halo a four-collimator scheme was developed at turn six, which is around 1.9 MeV/amu. With the four-collimator scheme in place, simulations were carried out for 1 and 5 mA and two conceivable bunch lengths of $\pm 5^\circ$ and $\pm 10^\circ$ of the H_2^+ beam. The results with respect to the beam losses are given in Table 2 at the extraction septum. We conclude that, according to the experience of the PSI Injector II cyclotron, these values are acceptable.

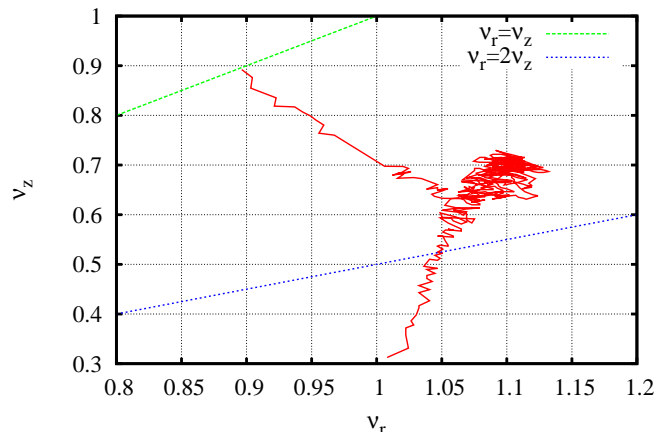


Figure 8: The betatron tune diagram in the DIC cyclotron

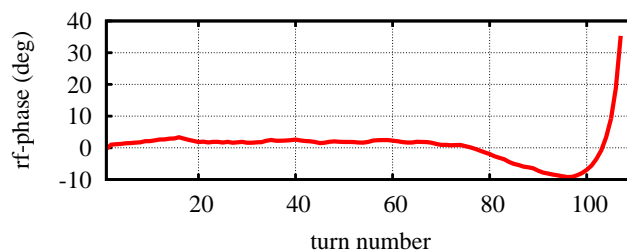


Figure 9: The integrated rf-phase shift in the DIC cyclotron

4.1. Extraction from the DIC

The turn separation of the concentric orbit is given as

$$\frac{dR}{dn} = R \frac{E_g}{E} \frac{\gamma}{\gamma + 1} \frac{1}{v_r^2} \quad (3)$$

Initial phase width	1 mA	5 mA
$\pm 5^\circ$	6 W	24 W
$\pm 10^\circ$	14 W	22 W

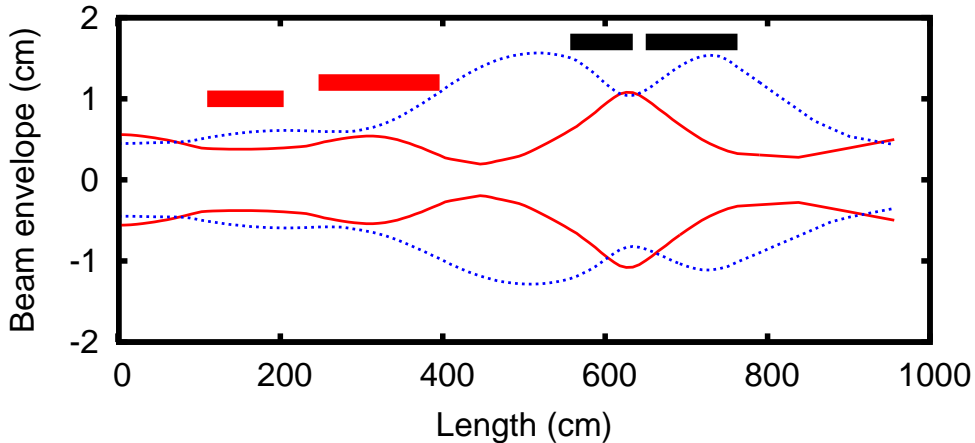


Figure 10: Radial (blue lines) and axial (red lines) beam envelopes along the extraction trajectory, with a uniform energy spread of $\pm 0.2\%$. The positions of electrostatic deflectors (ED1 and ED2) and magnetic channels (MC1-2) are also shown in red and black, respectively.

with R denoting the radius, E_g is the energy gain per turn, E is the total energy of the particles, γ is the relativistic factor, and ν_r is the radial focusing frequency [70]. The development of the turn separation is shown in Fig. 11; most importantly we get a turn separation of 20 mm at the extraction, which is enough for a clean extraction.

In Fig. 12 the radial profile of the last four turns are shown, at the center of the valley. In order to have enough statistics, we are using 10^6 macro particles in the full 3D simulation with space charge, similar to an earlier study [48]. The phase acceptance of the central region is not yet known; hence, we assume practical values of 10° and 20° . If the electric channel is inserted at $R=1.89$ m with an effective septum thickness of 0.5 mm, then the extraction efficiency is better than 99.9998% in the 5 mA case for both initial phases.

The first electrostatic deflector ED1 is placed in a valley, inside of one of the rf-cavities. This solution has already been proven in other cyclotrons and offer the advantages of being able to place the ED in a

Table 3: Parameters of the DAE δ ALUS Injector Cyclotron

E_{max}	60 MeV/amu	E_{inj}	35 keV/amu
R_{ext}	1.99 m	R_{inj}	55 mm
$\langle B \rangle @ R_{ext}$	1.16 T	$\langle B \rangle @ R_{inj}$	0.97 T
Sectors	4	Hill width	28 - 40 deg
Valley gap	1800 mm	Pole gap	100 mm
Outer Diameter	6.2 m	Full height	2.7 m
Cavities	4	Cavity type	$\lambda/2$, double-gap
Harmonic	6th	rf-frequency	49.2 MHz
Acc. Voltage	70 - 250 kV	Power/cavity	< 110 kW
ΔE /turn	1.3 MeV	Turns	107
ΔR /turn @ R_{ext}	20 mm	ΔR /turn @ R_{inj}	> 56 mm
Coil size	200x250 mm ²	Current density	3.1 A/mm ²
Iron weight	450 tons	Vacuum	< 10^{-7} mbar

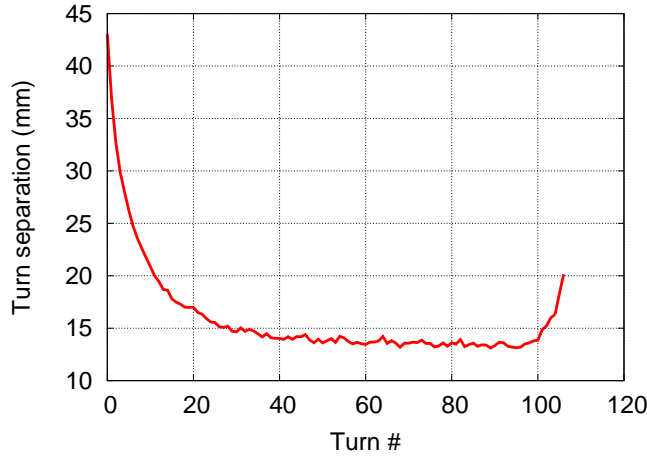


Figure 11: Turn separation of concentric orbits in the DIC. The radial gain is increased by about 7 mm without exceeding a phase slip of 50°

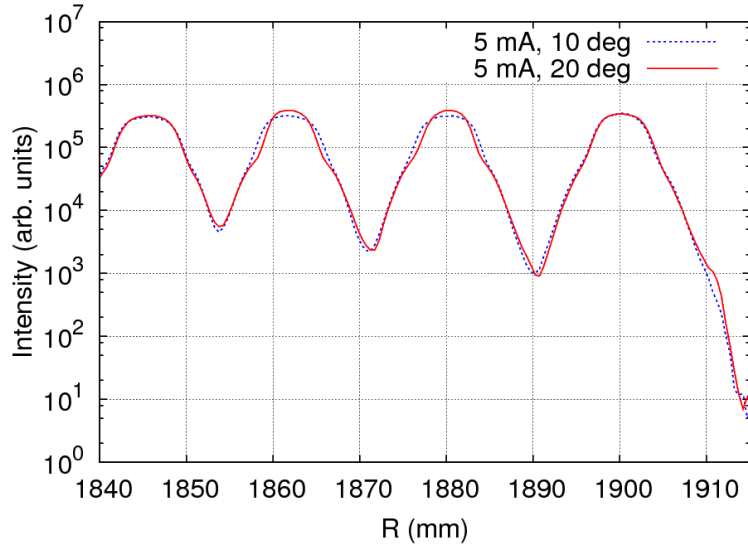


Figure 12: The radial profile of the last four turns at the center of the valley for a 5mA H_2^+ beam with the initial phase width of 10° and 20° , respectively

region where the magnetic field is low and there is enough room in the vertical direction. In Fig. 10 the positions of ED1, ED2, and of the two additional passive magnetic channels that guide the beam out of the cyclotron yoke, are shown. The ED1 length and its gap are 28° and 20 mm respectively, while the applied electric field is 30 kV/cm. The ED2 length and its gap are 40° and 24 mm respectively, while the applied electric field is 25 kV/cm. The first magnetic channel (MC1), 10° long, is placed 36° after the end of ED2, at the entrance side of the following hill. The MC1 produces a shielding of the local magnetic field of about 2.5 kGauss. The MC2 is 26° long and its shielding field is 4.4 kGauss. At the entrance of the first magnetic channel the separation between the accelerated orbit and the extracted trajectory is about 80 mm; hence, the two beams will be well separated. The radial and axial beam envelopes of the beam along the extraction trajectory are shown in Fig. 10. The initial radial size is about 10 mm and represents the beam core. The beam envelopes also include the effects due to the uniform energy spread of $\pm 0.2\%$. The initial beam size

was evaluated assuming a normalized beam emittance of 3.3π mm mrad. This value is about 30 times larger than the normalized beam emittance of the VIS.

5. The DAE δ ALUS superconducting ring cyclotron

The DAE δ ALUS Superconducting Ring Cyclotron is the main component in the accelerator chain. One of the big challenges again is beam loss, to be limited to a few hundred watts in total. This corresponds to relative beam losses in the lower 10^{-4} range. The choice of H_2^+ for the accelerated molecule species results in weaker space-charge forces and thus a higher intensity limit. However, the charge-to-mass ratio of 1:2 calls for high magnetic fields, posing the second challenge in the DSRC design.

The H_2^+ beam will be injected along the cyclotron valley by four injector magnets and one electrostatic deflector and it will be accelerated with four single-gap cavities. The extraction is performed by insertion of a pyrolytic graphite stripper foil with thickness less than 2 mg/cm^2 . Ionization through residual gas interaction of the beam contributes to the loss rate. A tentative layout of the DSRC is presented in the following sections. It includes the superconducting sector magnets, capable of generating sufficient field levels; the concept for the extraction foil in view of sufficient lifetime; and the overall design of the vacuum system that should provide pressure levels of $\approx 10^{-8}$ mbar. The main purpose of the present magnet design is to demonstrate the feasibility of the physics parameters, but we are also taking into account that full optimization, particularly in coil design, may require substantial changes to this baseline design.

5.1. The sector magnet for the DSRC

In the DSRC the main magnet configuration consists of eight superconducting sector magnets. Compared with a previous study [15–17], the parameters of the DSRC magnetic sector have been significantly improved with respect to the shape and current densities of the superconducting coils to improve focusing properties and reduce forces on the structure. The iron of the hill nearest to the median plane now has a strongly modulated shape to achieve stronger vertical focusing. A hole in the center of the hill has been introduced to adjust the average field. The minimum clearance between the lower and upper cryostat surfaces is now at 75 mm, and the gap between the poles is at 80 mm in order to achieve sufficient vacuum conductance. Figure 13 shows the iron and conductor package of one sector, and Table 4 shows the main parameters of the coils.

Table 4: The main parameters of the superconducting coils

Coil size near center (width x height)	$15 \times 48 \text{ cm}^2$
Coil size outer region	$24 \times 30 \text{ cm}^2$
I coil	3400 A/cm^2
Max. Field	6.18 T

5.1.1. Focusing properties

The isochronous magnetic field error is $\pm 0.4\%$, with sufficient focusing properties in both the radial and vertical planes. The ν_z is kept above 0.5 and the Walkinshaw resonance $\nu_r = 2\nu_z$ is crossed quickly and only once at the beginning of the acceleration, as shown in Fig. 15. The present baseline design still poses several technical challenges, which in the future may require adjustments to the design as presented.

Figure 14 shows the difference between the theoretical revolution frequency and the revolution frequency evaluated by the magnetic field map of the model presented here. The isochronism was evaluated by the orbit code Z4 [19]. The radial and vertical focusing frequencies ν_z and ν_r are shown in Fig. 15. The fast oscillations are due to the grid size of the magnetic field map used to evaluate the model.

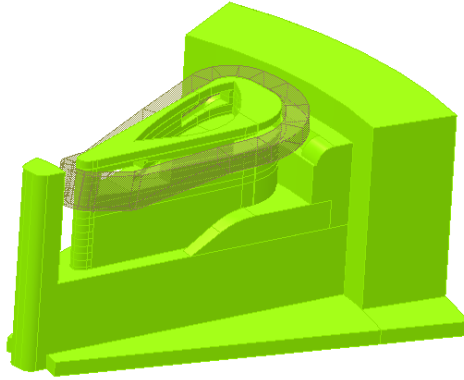


Figure 13: Drawing of the pole and the coil package

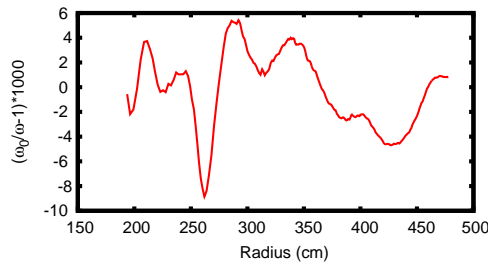


Figure 14: Relative difference between the ideal revolution frequency ω_0 and the revolution frequency ω of the particles.

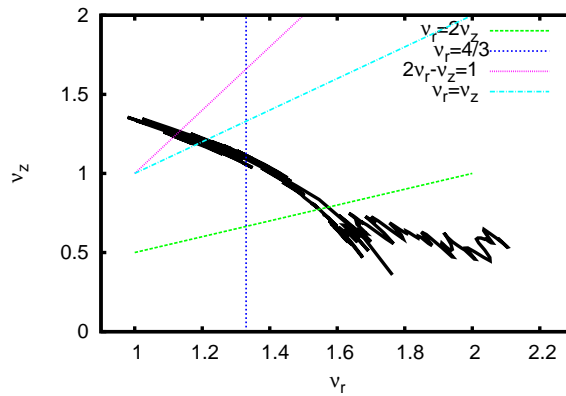


Figure 15: Tune diagram, ν_z vs. ν_r .

5.1.2. The analysis of magnetic forces

A detailed evaluation of the magnetic forces resulting in structural forces is made by using the code OPERA. The geometry and different sectors for the force evaluation are shown in Fig. 16. The maximum field on the coil surfaces is lower than 6 T for all conductor segments, except on segments number 3 and 4. In these segments, the peak field reaches 6.18 T. Strong expansion magnetic forces, which try to make the coil round, acting on segments 1, 2, 8, 9, 11, and 12. The strength of these forces, on the order of MN, is due to the high magnetic field and the large cross section of the coils. To compensate for these forces, different solutions have been evaluated. In the present design, the thickness of the LHe vessel varies. A thickness of 4

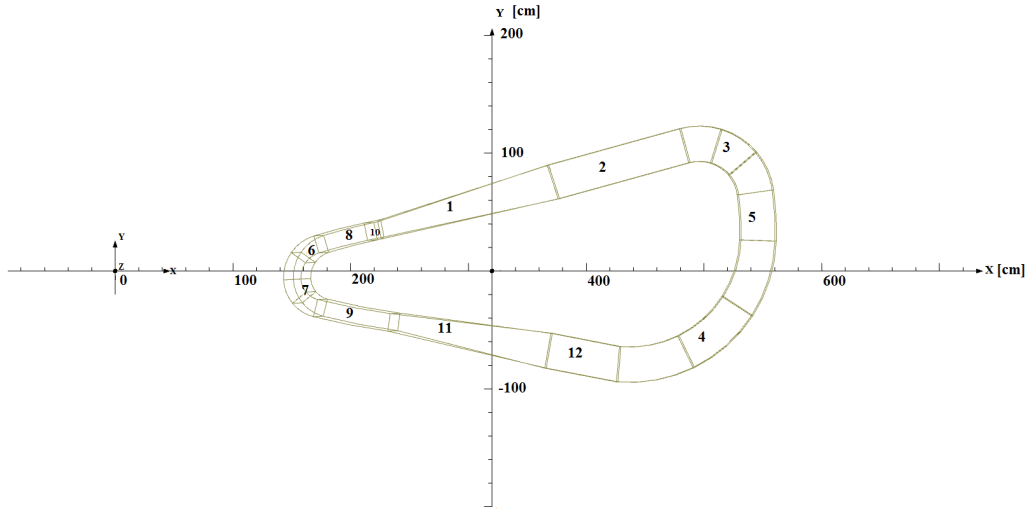


Figure 16: For the stress analysis, the superconducting coil is divided into 12 sections.

cm is chosen for the side near to the median plane and for the wall that is the nearest to the iron of the hill. The other wall and the side farther from the median plane are 7 cm thick. To optimize the magnetic field configuration, the cryostat wall that faces the pole has to be made of iron. The outer part that faces the valley and the median plane has to be stainless steel. The use of iron and stainless steel to build a cryostat has been already demonstrated.

An additional solution to the huge forces issue was suggested in [13, 14]. Opposite segments are connected by two stainless steel plates [15]. As the forces on the opposite segments of the coil have roughly the same magnitude but opposite directions, the residual force can be nearly canceled.

The thicknesses of the LHe vessel and of the connecting plates are chosen to maintain the stress values below 6 dN/mm^2 . The region between the LHe vessel and the cryostat walls is in a vacuum to guarantee the cryogenic insulation. The distance between the inner wall of the cryostat and the outer wall of the LHe vessel is fixed at 40 mm and it is sufficient to accommodate more than 30 layers of aluminized insulators.

To minimize the thermal load on the LHe vessel an intermediate shield, cooled to 77 K, is installed in the gap between the cryostat and the LHe vessel. Enough room is included above and below the cryostat for an elliptical cooling tube for liquid nitrogen.

The attractive magnetic force between two symmetrical coils, with are symmetrical with respect to the median plane, is large. It is on the same order as in the RIKEN SRC design. Also, in agreement with RIKEN, the present design assumes the coil segments 6 and 7 at the inner radii of the upper coil and the coil segments 3, 4, and 5 at the outer radii of the upper coil are connected with their corresponding segments of the lower coil by stainless steel plates, which are large enough to counterbalance this attractive force. Note that the parts of the cryostat corresponding to these segments are more solid than the ones corresponding to the other segments, which are sustained only by the structure of the LHe vessel.

In Table 5 we compare the main parameters of the DSRC magnet design with the parameters of the existing RIKEN SRC. Many parameters are similar; hence, they are creditable in lieu of a technical realization.

5.2. Radial injection into the DSRC

We assume the H_2^+ beam has an energy of 60 MeV/amu, an rms energy spread of 0.2%, and a normalized emittance of $10.0 \times \pi \text{ mm mrad}$ in order to match a beam-size similar to the one predicted by OPAL. The

Table 5: Comparison of the main parameters for DSRC with those for RIKEN-SRC

Basic Parameters	DSRC	RIKEN-SRC	Unit
Maximum field on the hill	6.05	3.8	T
Maximum field on the coil	6.18	4.2	T
Stored Energy	280	235	MJ
Coil size	30× 24 or 15× 48	21× 28	cm ²
Coil Circumference	9.8	10.86	m
Magnetomotive force	4.9	4	MA _{tot} /sector
Current density	34	34	A/mm ²
Height	5.6	6.0	m
Length	6.9	7.2	m
Weight	≤450	800	ton
Additional magnetic shield	0	3000	ton/total
Magnetic Forces			
Expansion	1.87 or 1.8	2.6	MN/m
Vertical	3.7	3.3	MN
Radial shifting	2.7	0.36	MN
Azimuthal shifting	0.2	0	MN
Main Coil			
Operational current	5000	5000	A
Layer × turn	31×16	22×18	
Cooling	Bath cooling	Bath cooling	
Maddock Stabilized Current	6345	6665	A
Other Components			
SC trim	no	4	sets
NC trim × turn	no	22	pairs
Stray field in the SRC valley region	0.7	0.04	T
Gap for thermal insulation	40	90@min.	mm
Extraction method	Stripper foil	Electrostatic channel	

main constraints of the injection scheme are the following:

- the axial beam envelope must be smaller than 5 cm (full width) in the region where the beam crosses the accelerating gap
- the beam has to match the equilibrium orbit at the matching point, which is chosen at $\theta = 180^\circ$ in the middle of the hill
- in order to bend the trajectory we plan to mainly use a passive magnetic channel. Normal conducting coils will be used to tune the fields.

To achieve these constraints, we track eigen-ellipses backwards from the matching point. The results of Z4 [19] simulations are shown in Fig. 17. Here the injection trajectories are shown together with the main components, the five passive magnetic channels (MC1-MC5) and the electrostatic deflector (ED). The trajectory crosses a field-valley with a rf-cavity installed however; the effect is a slight radial steering of the trajectory that can be compensated for by an external steering magnet.

MC2 is placed just inside a hole in the inner return yoke of the sector magnet and has to increase the shielding effect of the yoke by about -2 kGauss. MC3 stays in the inner fringing field and increases the local stray field to 11 kGauss. The most critical device is MC4, which has to produce a shielding effect of -13.8 kGauss. This large value can be achieved by using a passive shielding magnet and an additional normal conducting coil to produce a tuning field in the range of about -1 kGauss. The separation between the equilibrium orbit and the injection trajectory at the position of the magnetic channels is 4 cm at the

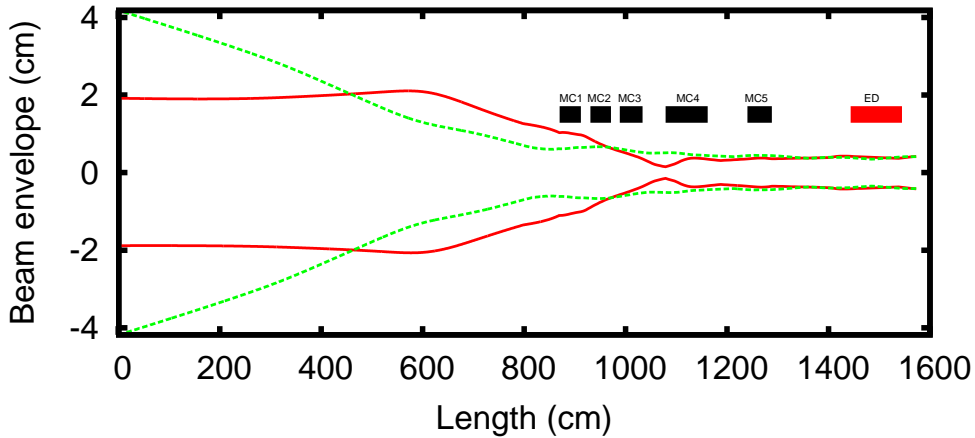


Figure 17: Vertical (green) and radial (red) envelope along the injection trajectory, computed using the OPERA code until ED. From ED to the electrostatic deflector the core Z4 [19] is used.

minimum. In particular, the orbit separation exceeds 20 cm at MC3 and MC4, the channels that need higher magnetic fields.

The separation between the injected beam and the first accelerated orbit at the position of the ED is about 2 cm. This distance could be increased up to 3 cm by injecting the beam slightly off-center. This first harmonic should produce a beam oscillation which increases the separation up to 3 cm at the position of the ED. The deflecting voltage of the electrostatic element is at a conservative value of 50 kV.

5.3. Stripper extraction

The stripping method utilizes a thin pyrolytic graphite foil, highly oriented, with a thickness of about 2 mg/cm^2 . By interaction with the foil, the molecule dissociates into two protons which follow an orbit with different curvature due to their charge-to-mass ratio of one. The stripping extraction has an efficiency close to 100%, even if the beam orbits at the extraction radius are not well separated. A disadvantage is the relatively high energy spread of the extracted beam due to overlap of several turns on the foil. According to OPAL simulations, an energy spread of 1.2% is expected.

Figure 18 shows the extraction trajectory. The stripper foil is placed on the entrance edge of the hill, allowing us to safely extract a small fraction ($< 10^{-4}$) of neutral hydrogen particles that are produced during the stripping process. The beam envelope vs. beam trajectory length is shown in Fig. 19. This figure shows the radial and axial beam envelope for the 800 MeV proton beam with and without $\pm 1.0\%$ energy spread. The axial beam envelope does not change significantly due to the energy spread. The maximum radial beam envelope due to the energy spread is $+5 \text{ cm}/-4.5 \text{ cm}$. At the exit of the cyclotron, the radial width of the beam envelope is less than 3 cm. The trajectories originate on the stripper foil placed at $R = 488.3 \text{ cm}$ and at the azimuth angle of 215° . The beam envelopes in the radial and axial plane were obtained from the eigen-ellipses evaluation. The normalized emittance is assumed to be $10 \times \pi \text{ mm mrad}$ (corresponding to 100% of the beam), and again roughly 100 times larger than the ion source emittance.

At the position where the trajectory is nearest to the center of the cyclotron, it is possible to install a magnetic channel to steer the trajectory and to provide axial focusing in order to maintain the vertical beam envelope below 4 cm along the trajectory inside the vacuum chamber. The angular extension of the magnetic channel is 10° , inside an empty valley. The bias field of the magnetic channel is 0.1 T and its radial gradient is 0.1 T/cm. The maximum size of the beam inside this magnetic channel is about 8 cm. The stripper foil azimuth position was chosen to stay in the region where the magnetic field is in the range 0.2 to 0.4 T. The bending radius of the stripped electron will be ~ 8 to 9 mm; hence, these electrons can be stopped easily on a copper shield.

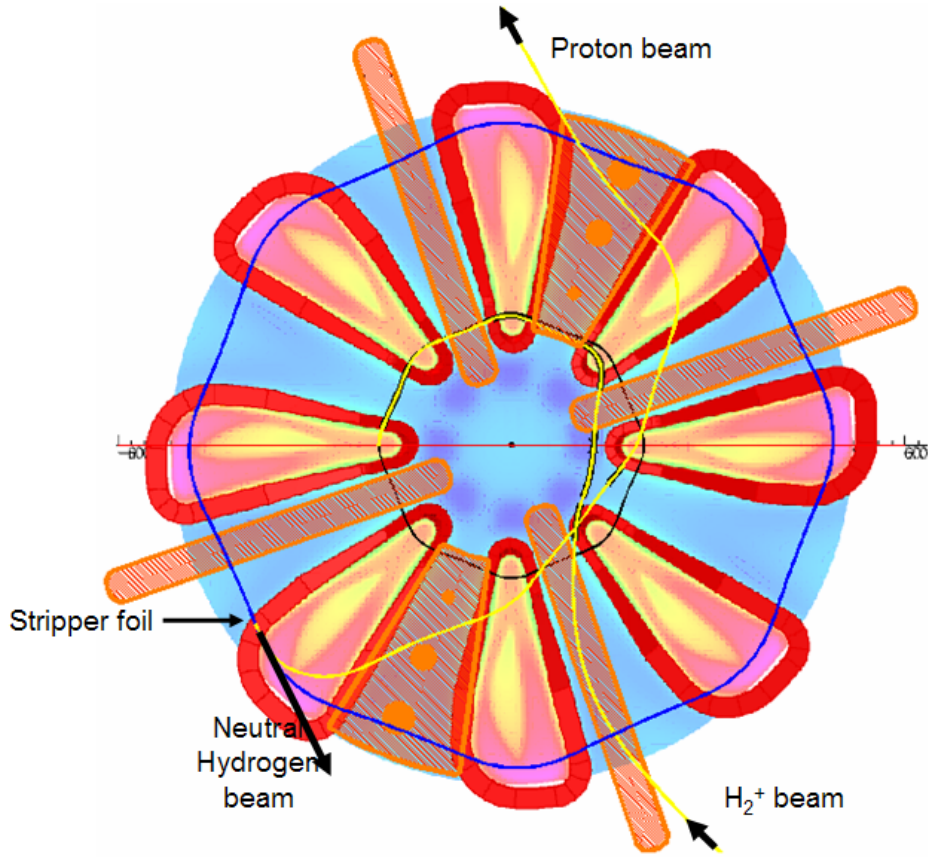


Figure 18: Injection and extraction scheme of the DSRC. The extraction trajectory for the proton beam with an energy of 800 MeV and the injection trajectory of H_2^+ with an energy of 60 MeV/amu are shown as yellow trajectories. The stripper is placed at an angular position of 215° . The magnetic channels along the injection trajectory and the extraction trajectory are indicated.

5.4. Stripper foil considerations

At the outer radius of the DSRC, H_2^+ ions are dissociated into two protons by a carbon stripping foil and are led into the extraction channel that snakes through the central region of the DSRC. Various considerations are important: a) foil type, shape, thickness, and mounting technique; b) foil lifetime; and c) stripping efficiency.

5.4.1. Foil type

Substantial experience exists with strippers for high-current beams for stripping of H^- from machines such as TRIUMF, Spallation Neutron Source (SNS), and commercial (lower-energy) isotope-producing cyclotrons. TRIUMF utilizes 2 mg/cm^2 highly oriented pyrolytic graphite foils for their 520 MeV beam, supported on an inverted L-shaped frame which is in turn also supported on two edges so as to minimize mechanical constraints from foil changes due to thermal cycling and aging. In addition, clamping the carbon stripper, a tantalum frame that is lined with thin, wrinkled copper foil helps reduce mechanical stresses [35]. SNS strips 1 GeV ions using $260 \text{ } \mu\text{g/cm}^2$ polycrystalline diamond foils supported only from the top edge, thinner foils being required to minimize scattering due to multiple passes of the stripped beam during stacking in the accumulator ring [36]. Commercial isotope cyclotrons for 30-70 MeV H^- use 200-400 $\mu\text{g/cm}^2$ pyrolytic graphite supported on a C frame.

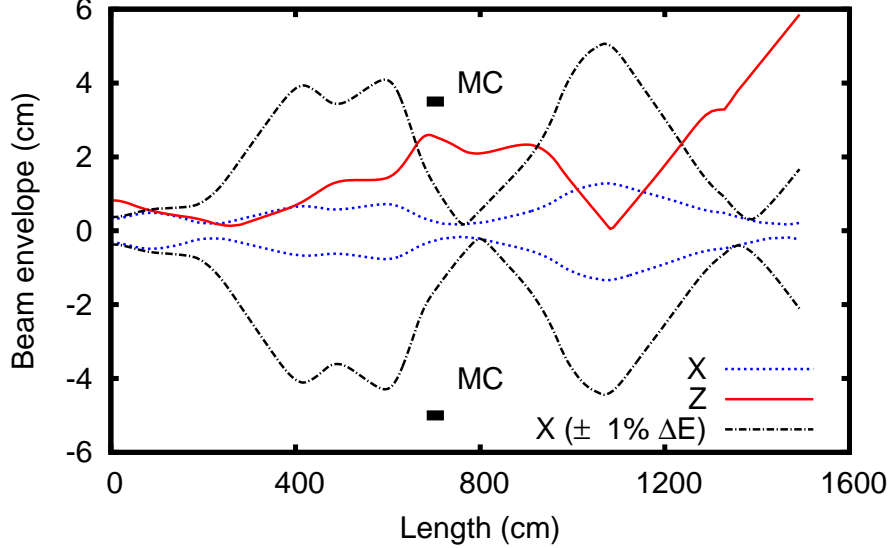


Figure 19: The radial (blue lines) and axial (red line) envelopes for the proton beam with zero energy spread vs. distance from the stripper position along the extraction trajectory are shown. The black line indicates the radial beam envelope for an energy spread of $\pm 1\%$. The position of the steering magnet channel (MC) is indicated as black boxes.

5.4.2. Foil temperature & lifetimes

The foil lifetime is highly dependent on the average and instantaneous power deposition from the beam, and on the trajectory of electrons stripped from the primary ions. Furthermore, the pulse structure can have a substantial impact on the peak foil temperature, as radiative cooling time constants play an important role. Ultimately, the peak temperature in the foil determines its lifetime, and temperatures above 2500 K lead to rapid failures due to sublimation. Generally, the lifetime is inversely proportional to the beam intensity, given that the foil temperature is low. In fact, foil lifetimes are affected by thermionic emission as well, which becomes appreciable at temperatures even below 2000 K (where graphitization starts); hence, controlling peak temperatures is of great importance.

Instantaneous power is assumed to be a factor of 5 over average power operating at a duty factor of approximately 20%. The foil temperature θ_{foil} was calculated by integration of the following equation:

$$\frac{d\theta}{dt} = \frac{1}{\tau\rho c} \times (\omega - 2\sigma\epsilon\theta^4),$$

$$\theta_{foil} = \theta + \theta_{circ}$$

where all the variables and constants are defined in Table 6. The average power density during beam on can be estimated to be about 1 W/mm^2 , assuming that beam profile is uniform; however, a ω of 3 W/mm^2 was used from the beam profile at the extraction foil (Fig. 22). The left graph in Fig. 20 shows a temperature evolution in the cases of pulse widths of 0.01 ms and 1 ms. In the case of 0.01 ms, the temperature is determined by the average beam power. In the case of 10 ms, we observe large temperature fluctuations with a peak temperature at 2500 K. The right graph in Fig. 20 shows the foil maximum temperature as a

Table 6: Estimation of the foil temperature for a foil thickness of 2 mg/cm^2 and 1 mg/cm^2

Quantity	foil thickness 2 mg/cm^2	foil thickness 1 mg/cm^2	Unit
Energy loss	0.0044	0.0022	MeV
Peak current H_2^+	5	5	mA
Duty cycle	20	20	%
Pulse width	$0.1 \sim 1000$	$0.1 \sim 1000$	ms
Beam Area (4 x rms)	10	10	mm^2
Foil thickness \times density $\tau\rho$	2	1	mg/cm^2
Specific Heat c	8.5/12	8.5/12	J/g K
Max. power density during beam-on ω	10	5	W/mm^2
Emissivity ϵ	1	1	
T circumference θ_{circ}	303	303	K

function of pulse width, from $0.01 \dots 10$ ms. From the graph it is obvious that the pulse width should be less than 1 ms to keep the foil temperature at acceptable levels.

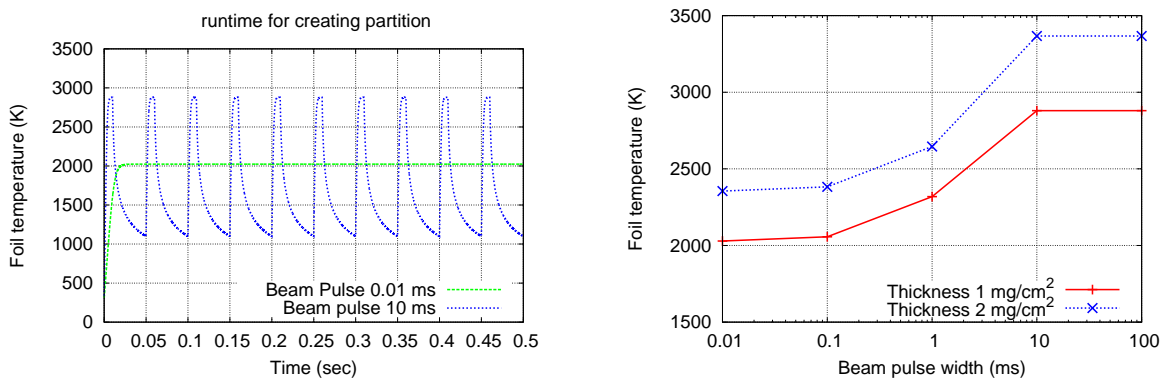


Figure 20: Thermal cycling in the foil vs. pulse width: shorter pulses lead to much more regular foil heating (left figure). Maximum foil temperature vs. pulse width. The knee is at about 1 ms pulse width, at a rate of 200 Hz (right figure).

Energy deposition on the foil can be severely affected by the orbits of convoy electrons. These stripped electrons carry an energy of about 440 keV each, so contribute an average power of 272 watts per megawatt of protons. If the foil is placed in a strong field, the electrons spiral around and deposit this energy into the foil. To control this, the plan is to place the foil in the fringe-field of a sector magnet, where the strength is about 0.2 T, so the electron orbital radius is about 1 cm. As the electrons are bent towards the outside, a cooled electron catcher can be placed to intercept them.

The performance experience of SNS can be taken as an indication that acceptable foil lifetimes are well-within current technology. The SNS runs at a 6% duty factor, with 1 ms beam on and 16 ms beam off, and an average power of 1 MW (17 MW peak power). The Chemical Vapor Deposited (CVD) polycrystalline foils have operational lifetimes of several months [34, 36]. Possible reduction of foil thickness to account for what is expected to be more efficient stripping of the one electron from H^- as compared to the two from H_2^+ (one which is rather tightly bound), could lead to a reduction in energy loss (power deposition) in the foil, and even longer lifetimes.

5.4.3. Stripping efficiency

Incomplete stripping can lead to beam loss at high energy, and if not mitigated, will be a major contribution to the power-loss budget of the DSRC. Incomplete stripping occurs when the primary beam misses the foil, or if ions emerge either as unstripped H_2^+ or H_0 . The foil size will be a few cm^2 , and will cover the full vertical height of the beam. In the radial dimension, the foil will cover the last several turns; hence, the probability of an ion not intercepting the foil is vanishingly small. Furthermore, if an ion misses the foil (on its inner edge), it will intercept the foil on its subsequent turn.

A foil thickness of several hundred $\mu\text{g}/\text{cm}^2$ is sufficient to break up all molecular ions passing through it. Consider now the extremely unlikely event of an intact (not stripped) ion that emerges from the foil; in that case the energy loss of this ion is about $\frac{1}{2}$ MeV per mg/cm^2 of foil thickness, which is substantially less than the energy gain per turn, so the ion will intercept the foil again on its subsequent turn.

Neutral hydrogen is a significant problem in stripping H^- ; at SNS they observe about 3% of their beam emerging from the stripper as H_0 . A non-negligible fraction of these neutrals are in weakly bound, long-lived (metastable) Rydberg states. The fraction of neutrals is expected to be substantially lower for H_2^+ , as there is only one electron to remove, whose (ground-state) binding energy is 2.7 eV; while the H^- ion has two electrons. The most loosely bound at 0.7 eV is easy to strip, but the second electron, with a binding energy of 13.6 eV may be more difficult to cleanly remove.

Mitigation of the neutral components is relatively straightforward; ground-state neutrals will follow a straight-line trajectory from the stripper, and a dump can be placed at the point where these atoms exit the magnet yoke. These ground-state neutrals will safely traverse even the strongest magnetic field region, because the binding energy is such that Lorentz stripping of these atoms is essentially impossible. However, the weakly bound metastable neutrals will undergo Lorentz stripping when traversing any appreciable magnetic field, resulting in a contribution to beam halo in the extraction channel. However, the acceptance of the DSRC extraction channel is large, and simulations have indicated that all such halo particles will be extracted cleanly, as long as the magnetic field stripping these atoms is sufficiently close to the stripper foil.

5.5. Vacuum system

Due to interactions with the residual gas, ions can lose their orbital electron as they travel along the acceleration path. The fraction of beam particles which survives acceleration is given by [27]

$$T = N/N_0 = \exp(-3.35 \cdot 10^{16} \int \sigma_L(E) P dL), \quad (4)$$

$$\sigma_L(E) \approx 4\pi a_0^2 (v_0/v)^2 (Z_t^2 + Z_i)/Z_i \quad (5)$$

where P is the pressure (torr) (3.35×10^{16} is the number of molecules/ cm^3 in one Torr), L is the path length in cm, and $\sigma_L(E)$ is the cross section of electron loss. The ion velocity is denoted with v , v_0 and a_0 are the characteristic Bohr velocity and radius and, Z_t & Z_i are the atomic number of the residual gas and of the incident ion respectively. While this formula is in good agreement with experimental data, its accuracy is not demonstrated for energies higher than 100 MeV/amu

Assuming that the distribution of vibrational states of H_2^+ is sufficiently cold that the Lorentz-force induced dissociation is negligible, scattering of beam ions on the residual background gas will be the primary beam loss mechanism during the acceleration process. Therefore, keeping the total beam power lost in the DSRC to 200 W or less requires that the vacuum chamber remains at ultra-high vacuum conditions (≤ 10 nTorr) despite the presence of a MW-class beam.

From Table 10.2 of [8], the electrical current lost in the DSRC due to beam-gas collisions is

$$I_{ions} = \frac{I_{ave}}{2 \text{ mA}} \frac{P}{10 \text{ ntorr}} 1.25 \mu\text{A}, \quad (6)$$

where I_{ave} is the average current in a macro pulse and P is the gas pressure in the vacuum chamber. Converting this to protons lost per second we get the following scaling relation,

$$\frac{dN_{beam}}{dt} = \frac{I_{ave}}{2 \text{ mA}} \frac{P}{10 \text{ ntorr}} 7.25 \times 10^{12} \text{ ions/s.} \quad (7)$$

For the nominal parameters, the energy deposition is 7.25×10^{12} ions/s $\times 8 \times 10^8$ (eV) $\times 1.6 \times 10^{-19}$ = 560 W which is too high by a factor of two. However this value is computed from the peak current derated by the duty factor. With respect to the pumping requirements which is probably pessimistic since the diffusion times for residual gas are relatively high – thus the pressure peak smears out. It is also evident, that with respect to the peak current the gas load is dominated by thermal outgassing. As the number of protons hitting the walls determines the activation of the chamber, as well as the dynamic gas load, a prudent choice may be to reduce the baseline pressure to 5 nTorr.

A critical engineering parameter in the design of the vacuum system is the effective ion-induced desorption coefficient, defined as

$$\eta_{eff} = \frac{\text{number of molecules desorbed}}{\text{number of incident ions}}. \quad (8)$$

The incident particles that produce the dynamic gas load, Q_{dyn} , can come both from the beam itself and from the fragments of residual gas that has been ionized by the beam and accelerated by the electromagnetic fields of the beam into the walls. If the vacuum system is free of leaks and if all seals are metal-to-metal except for the sliding seals between the rf-cavities and the beam chamber, the thermal out-gassing of the vacuum chamber walls, Q_0 will provide the only static gas load in the absence of beam. For an unbaked vacuum chamber, Q_0 may be as large as 2×10^{-10} Torr-l/s/cm². The four rf-cavities introduce an additional area of $\sim 1.5 \times 10^6$ cm². As the cavities are run well above room temperature (assume T = 70 C), the out-gassing in these cavities may be as high as ~ 20 times larger than in the vacuum chamber. Consequently the total static load is 3.2×10^{-4} Torr-l/s. The dimensionless ion-induced desorption coefficient, η_{eff} , depends strongly on the angle of incidence of the ion and on the ion energy. Relevant measurements of the ion-induced desorption by protons have been reported by the CERN vacuum group. [32, 33]. The value is ~ 10 for the gases mostly commonly found in ultra-high vacuum systems. To be very conservative one might double these values of η_{eff} because the desorption coefficient will be larger before the walls are scrubbed by impacts from lost beam particles.

Therefore, the dynamic gas load¹ in the system is

$$Q_{dyn} = \eta_{eff} [I_{ave}/2 \text{ mA}] \times [P/ 10 \text{ ntorr}] \times 4.1 \times 10^{-7} \text{ torr-l/s}, \quad (9)$$

and consequently, the total gas load reads: $Q = Q_{dyn} + Q_0$. The pumping speed, S , required to maintain the cyclotron at a pressure, P , in the presence of the gas load due to ion-induced desorption is

$$S = \frac{Q}{P} = \eta_{eff} \{ [I_{ave}/2 \text{ mA}] \times [P/ 10 \text{ ntorr}] \times 4.1 \times 10^{-7} + Q_0 \} \times 10^8 / [P / 10 \text{ ntorr}] [\text{l/s}]. \quad (10)$$

With proper preparation of the chamber, we expect the value of η_{eff} to be ≈ 20 for H_2^+ . Assuming that for 1 to 10 ms pulses we must use the peak current in place of I_{ave} ,

$$S = [I_{peak}/2 \text{ mA}] \times 8.2 \times 10^2 + 32000 [1/s P / 10 \text{ ntorr}] \approx 4 \times 10^4 [\text{l/s}] \quad (11)$$

a number that is well within the capacity of sorption pumps.

One attractive choice, which is effective at pumping hydrogen, would seem to be a cryopanel operating at 4.2 K. Measurements of a porous carbon panel at TRIUMF [4] achieve a pumping rate of $1.2 \text{ l s}^{-1} \text{ cm}^{-2}$; a CERN system using a silver coated surface does much better, delivering $9.2 \text{ l s}^{-1} \text{ cm}^{-2}$. As the coverage of hydrogen builds up on the cold surface, the equilibrium vapor pressure of H_2 will increase well beyond 10 nTorr. Therefore maintaining the pressure at 10 nTorr would require running the cryopanel in each sector magnet with an area of 1000 cm² each at ~ 3.5 K. An alternative used successfully at RIKEN is using high capacity cryopumps. These have the advantage of being placed in areas of maximum gas-load, thereby minimizing the reduction of effective pumping speed due to limited conductance such as in the rf-cavities. Using eighteen pumps each of $\sim 10^4$ l/s, the RIKEN-SRC, which has a larger vacuum chamber surface area

¹1 molecule/s = 2.83×10^{-20} torr-l/s

than the DAE δ ALUS design, obtains a base pressure of < 10 nTorr. The pumps are regenerated every four to six months.

An advantage of using the RIKEN approach is that high-capacity pumps can be placed directly at the top and bottom of the DAE δ ALUS rf-cavities, which will be similar to the PSI design. As the rf-cavities constitute the largest fraction of the surface area in the vacuum system, this placement of pumps will be highly effective.

One region of concern is the area near the carbon stripping foils for extraction. If one loses 0.02% of the beam in this region similar to the losses near the septum in the PSI machine the resulting dynamic load would be $Q_{dyn} \sim 2.3 \times 10^{-6}$ Torr-l/s.

5.6. Space-charge-effects

For DSRC cyclotrons, single bunch space-charge effects are not the only contribution. The radial turn separation at injection is 27 mm and gradually reduces to about 3 mm at the extraction. In consequence, the beam size at the outer radii can be larger than the radial separation, and radially neighboring bunches will partially overlap.

This simulation starts with an initial centered beam of 60 MeV/amu at injection. In order to evaluate the influence of space charge, simulations are done for the beam currents of 1 and 5 mA. The initial transverse rms emittance $\epsilon=0.9 \pi$ mm-mrad (normalized) and the initial phase width and energy spread are set to a practical value of 10° and 0.6%, derived from the PSI operational experience.

The simulation result shows the vertical beam extension induced by space charge and neighboring bunch effects is small. For the 5 mA current, the beam halos extends vertically to 60 mm (full width). Considering the hill gap of the DSRC at 80 mm (full width), the beam is well separated from the magnet sector and vacuum chamber. There remains enough space for the vertical beam envelop fluctuations caused by a possible mismatch of the injected beam.

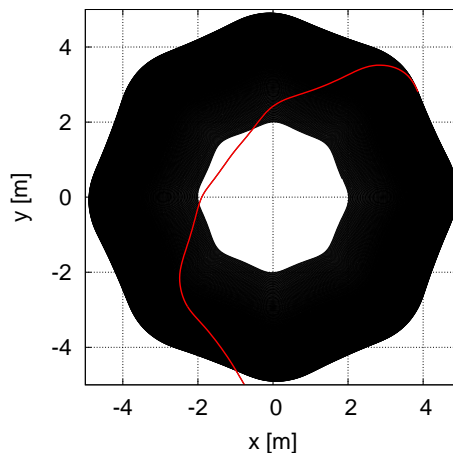


Figure 21: The H_2^+ acceleration trajectory (black) and proton extraction trajectory (red)

For cyclotrons using a multi-turn extraction scheme, obtaining the particle distribution at the stripper is critical because it constitutes the initial conditions for the subsequent beam transport in the extraction channel. For the DSRC cyclotron this is especially important because the protons in the extraction channel have the same sign of charge but a double charge-to-mass ratio than the H_2^+ particle. Protons will travel inwards guided by the complicated magnet and rf-fields, as is shown in Fig. 21. In Fig. 22 we show the radial profile and energy spread on the stripper. In this initial study, we neglect scattering on the foil itself, as well as the dynamics of the stripped electrons. For the 5 mA beam we find that the energy spread stays at $\pm 0.6\%$ at a phase width of 12° . The transverse normalized rms emittance are $\epsilon_{r,n}=1.1$ mm-mrad and

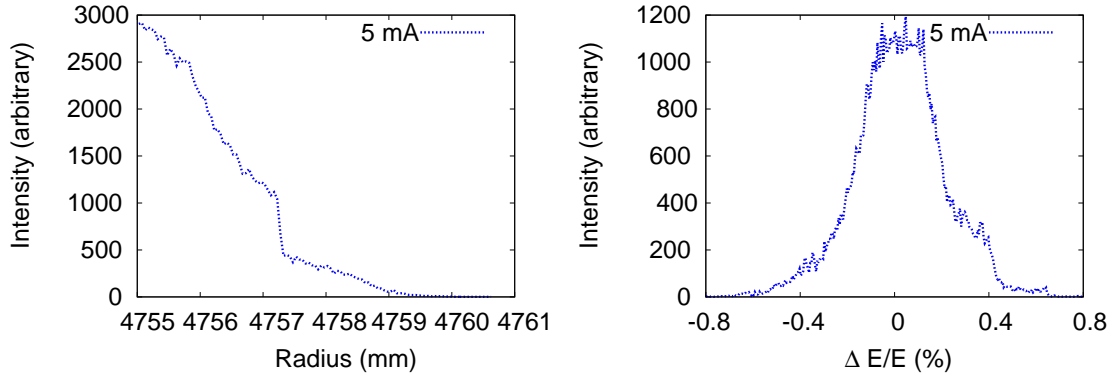


Figure 22: The radial profile and energy-spread-histogram of the H_2^+ 5 mA beam on the stripper.

$\epsilon_{z,n}=1.4$ mm-mrad. We take this result as the initial distribution for proton extraction simulation, which shows no problem for the beam transport in the extraction channel.

Detailed discussion of the space-charge effects in the DSRC cyclotron will be addressed in a forthcoming paper [71].

6. Radio frequency design

Focusing at the problem of vacuum and rf-voltage leakage at very high electromagnetic fields, we pose the question if the use of 8 double gap rf-cavities could be advantageous over a solution with 4 single gap rf-cavities. The double gap rf-cavities have the following advantages:

- It is possible to install a cryopanel inside the electrodes of the double gap cavities, near to the median plane and well shielded from the beam (4-10 cm far from the median plane). In consequence we have a large cryopanel in each valley.
- The maximum voltage could stay around 300 kV; hence, the problem of the rf-stray fields should be significantly reduced.
- The accelerating voltage is more uniform vs. orbit radius and of 4000 keV/turn at all the radii, while if we have only 4 single gap cavities we have a maximum of 4 MV just in the range 4.0 - 5.0 m.

6.1. DIC rf-design

The rf-cavity system of the DAE δ ALUS Injector Cyclotron consists of four double-gap cavities ($\lambda/2$ resonators) with one stem, that produce an energy gain of 0.5 MeV per cavity at the extraction radii (1900 mm) allowing the acceleration of the beam up to 60 MeV/amu. Double-gap cavities are suitable for applications in which a special radial voltage profile (along the acceleration gaps as shown in Fig. 24) is desired. The rf-voltage must not exceed 400 kV per gap, limiting the acceleration performance and requiring a complex cooling system. The double-gap cavity solution was modeled using the multi stem approach [24], the CAD-geometry is shown in Fig. 23. Double-gap cavities can be easily installed in the valley, they allow the insertion of cryo-pumps or cryo-panels adjacent to the median plane, an advantage with respect to increasing the performance of the vacuum system. Electrostatic deflectors can be installed at the extraction radius inside the dee if necessary, which shape will provide the required space.

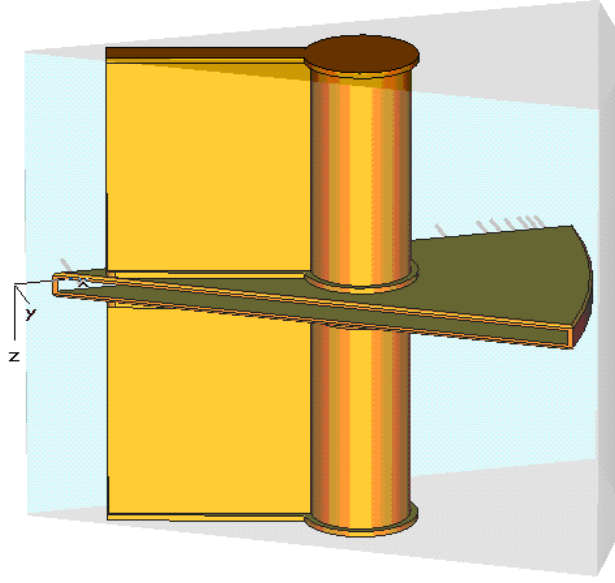


Figure 23: CAD geometry for the DIC rf-cavity

Table 7: Parameters and performances of the DIC double-gap cavity

	Injector Cavity	Unit
Cavity Height	1700	mm
Cavity Angular Extension (Width)	32	deg
Cavity Radial Extension (Length)	2100	mm
Dee Angular Extension (Width)	30	deg
Dee Gap	50	mm
Dee Thickness	20	mm
Stems Radial Extension	320-1330	mm
Stems Angular Extension	70	mm
Resonance mode	double-gap, $\lambda/2$	
Resonance frequency	49.2	MHz
Quality factor	9100	
rf-Power Dissipation	160	kW
Energy Gain (voltage distribution see Fig. 24)	70-250	kV
Max Surface Current	160	A/cm
Max Electric Field	6.1	MV/m

The cavity is a resonator with one stem that is connected to the liner and the dee by means of a system of flanges. The shape of the dee and the shape of the stem were optimized to fit the space requirements and to satisfy the rf-specifications. Table 7 lists the main parameters of the injector double-gap cavity.

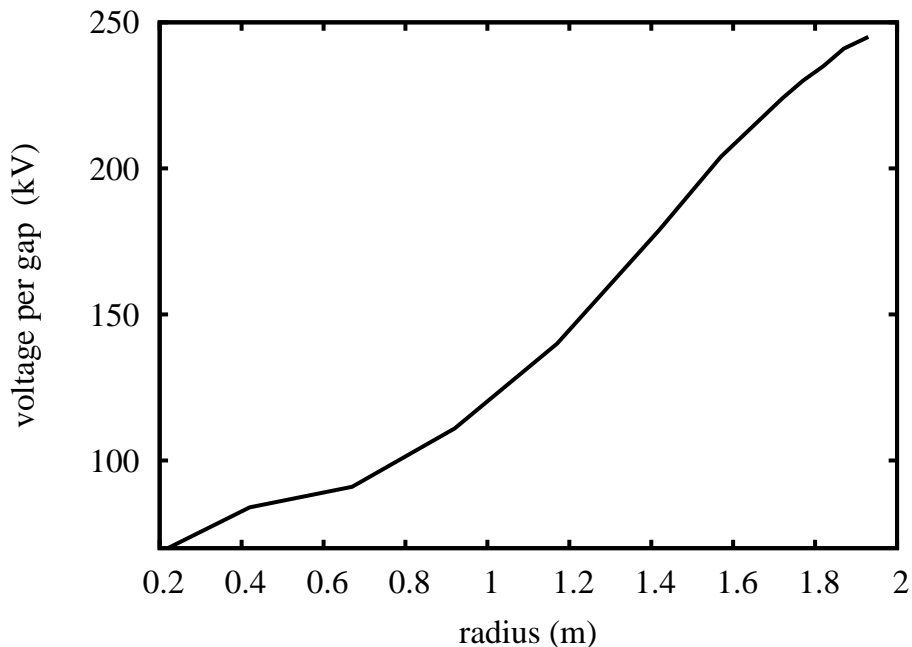


Figure 24: Gap voltage distribution in the DIC rf-cavity as function of the cyclotron radius.

Rf-power will be fed to the cavity via a capacitive coupler, frequency tuning pistons will be located in the same area.

6.2. DSRC rf-design

The rf-cavity system of the DAE δ ALUS Superconducting Ring Cyclotron consists of four single-gap cavities that are similar to the PSI box shaped cavities and produce an energy gain of 4 MeV per turn at extraction radii (4900 mm). Because of the large energy gain and the resulting decrease in acceleration time, the beam losses due to the interaction with the residual gases are minimized. Double-gap cavities (multistem $\lambda/2$ resonators) represent a valid option and are sketched briefly.

6.2.1. Double-gap cavities

Unfortunately it is not practical to install more than four single-gap cavities in an 8-sector cyclotron due to the mechanical interference of the cavities in the central region and the space needed for other elements. Therefore, despite the double gap cavities being less efficient than the single gap cavities, two double gap cavities can be added to increase the energy gain per turn by an additional 0.8 MeV, thus increasing the maximum beam power of about 20%, without increasing beam losses.

6.2.2. Single-gap cavities

Single-gap cavities can reach higher accelerating voltages (with sinusoidal distribution), and are less sensitive to higher-order modes. The cooling system, braised onto the outside of the cavity, is simple to fabricate with no risk of water leaking into the vacuum (high reliability) [23]. Engineering complexity and bigger dimensions are issues, but proven to be manageable, as shown at PSI. A single-gap cavity with a gradually modulated section along the radius was designed and optimized to fulfil the performance

requirements. The cavity wall consists of an 8 mm copper sheet on which cooling channels are directly tungsten inert gas (TIG) brazed. A large number of channels provides efficient water-cooling with small thermal gradients. The total height of the cavity is 3000 mm. The cavity radial extensions is from radius 900 mm to radius 7700 mm while the acceleration gap ranges from 150 mm to 300 mm (the acceleration is realized from radius 1900 mm to 4900 mm). The power will be fed into the cavity by two high power inductive couplers. A stainless steel support structure is required to provide mechanical stability to the cavity. The tuning of the cavity will be performed by means of the trimming system currently used at PSI [22]. This complex but effective cavity tuning system is realized by hydraulic tuning yoke that squeezes the cavity to compensate the frequency variation. No parallel surfaces represent a valid solution to avoid multipactoring. Four cryopumps located two per side of the cavity will provide the required 10^{-8} mbar vacuum. The vacuum between the cavity and the vacuum chamber of the coils is guarantee by a system based on inflating seals and by o-rings; this technology has been successfully developed and optimized at PSI and RIKEN [18]. Figure 25 shows a 3D model of the cavity, in Table 8 the main parameters of the DSRC single-gap cavity are compared to the existing PSI single-gap cavity.

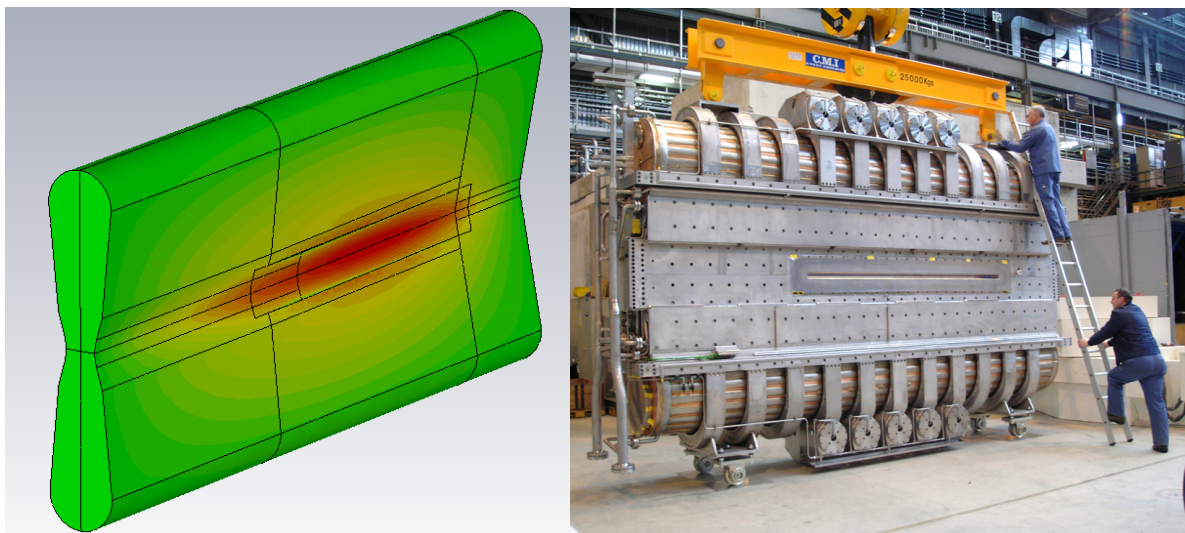


Figure 25: Electric-field distribution in the DSRC cavity (left) and existing PSI cavity (right).

The DSRC resonator works at the sixth harmonic (resonant frequency of 49.2 MHz) with a quality factor (Q value) of 37,500, the gap voltage distribution is shown in Fig. 26. The cavity needs 0.5 MW of power to produce an accelerating voltage that ranges from 0.5 MV at the inner radii to 1 MV at the extraction radius. The acceleration gap at the inner radii is reduced from 300 mm to 150 mm to fit into the restricted space of the valley due to the cryostat of the superconducting coils.

Table 8: Comparison of the rf-requirements for DSRC and achieved performance at the PSI 590 MeV Ring Cyclotron.

	DSRC	PSI 590 MeV RC	Unit
Cavity height	3000	2928	mm
Cavity length	6800	5200	mm
Cavity opening in the beam plane (injection)	150	300	mm
Cavity opening in the beam plane (extraction)	300	300	mm
Cavity copper sheet thickness	8	8	mm
Material of rf-surface	OFHC Copper	OFHC Copper	
Material of support structure	316LN	316LN	
Resonance mode	TM011	TM011	
Resonance frequency	49.2	50.6	MHz
Accelerating voltage per turn at the inner radii	2.0	3.4	MV
Accelerating voltage per turn at the outer radii	4.0	4.2	MV
Voltage distribution on a gap	0.5-1.0	half-sine	MV
Amplitude stability		0.03	%
Phase stability		0.01	deg
Quality factor	37,500	44,200	
rf-Power Dissipation for 1 MV gap voltage	500	300	kW
Wall plug power AC/DC conversion efficiency	0.9	0.9	
DC / rf conversion efficiency	0.64	0.64	
rf / average beam-power conversion efficiency	0.67	0.55	

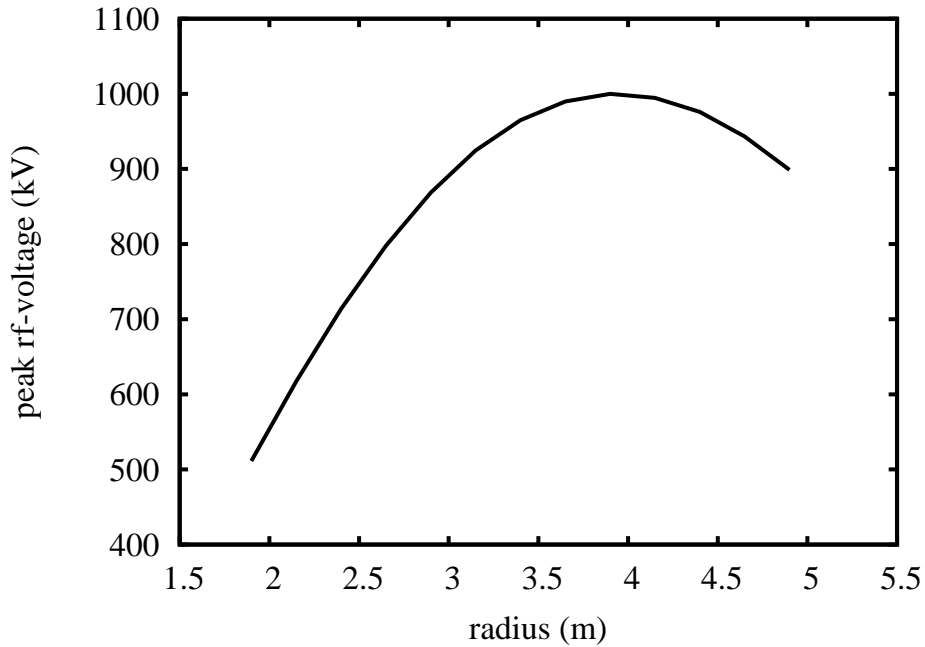


Figure 26: Gap voltage distribution in the DSRC cavity as function of the cyclotron radius.

6.2.3. Duty cycle

One of the challenges of the rf-system is the pulsed structure of the beam that is required for the final application, as shown in Fig. 27. The beam must be turned ON 20% of the time but the pulsing frequency could be selected in order to minimize the stress on the amplifier chains as well as the cavity voltage regulation. Another parameter to take into account is to minimize the global power consumption of the installation. For that it could be interesting to reduce the cavity voltage during the beam OFF times. Different scenarii have been analyzed from pulse lengths of $100 \mu s$ to a few seconds. The high Q value of the cavity defines a time constant of more than $200 \mu s$. In consequence, the filling time of the cavity would be at least $500 \mu s$ considering some overdriving. This probably rejects a pulse length of $100 \mu s$ or shorter. A pulse duration on the order of $1ms$ would allow us to reduce the rf-voltage during $3/5$ th of the time. In this case the mean rf-power is reduced by $1.2 MW$. This translates in a plug power reduction of nearly $2 MW$, considering the efficiency of the rf-amplifiers. A pulse of $10 ms$ would further reduce the power consumption by $600 kW$. An additional advantage is that the cavity cooling is greatly relaxed. Between $1 ms$ and $10 ms$ pulse duration, the tube power supplies can rely on their output filter bank to provide the peak power. The power supply can then be dimensioned to deliver only the average power.

One important point could also be related to the capability of the cavity voltage regulation to compensate fast enough for the beam loading.

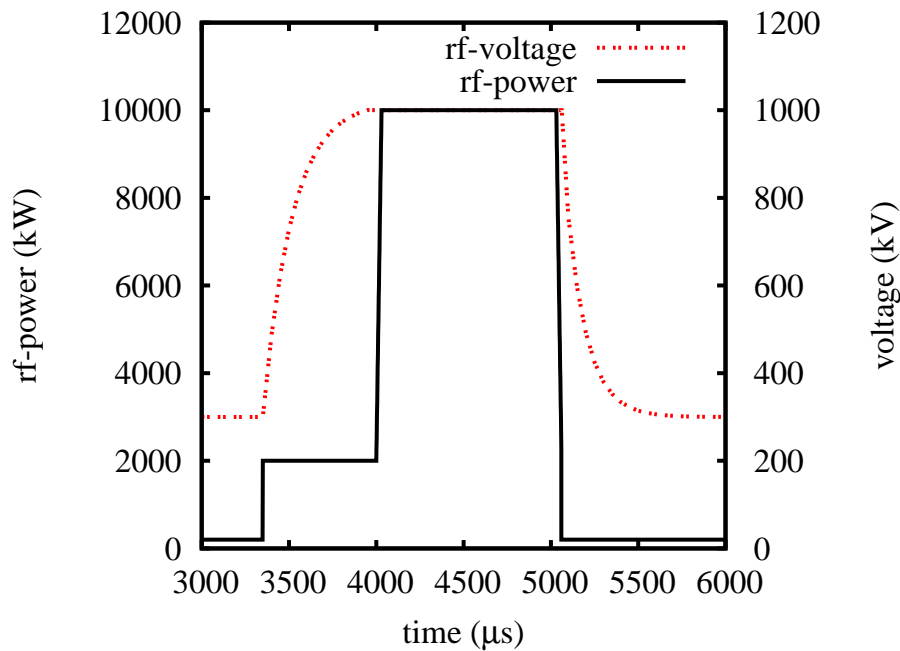


Figure 27: Example of a typical time-structure applicable for the DSRC rf-pulse.

The time for the beam to make the full acceleration in the ring cyclotron is about $30 \mu s$. This means that when the beam will be turned ON-OFF the required rf-power will rise-fall linearly during this time. This will naturally help the regulation loop to follow. In order to help the negative feed-back loop during the transients a feed-forward signal could be injected in order to anticipate the driving power requirement. Some examples of electrons accelerators with very large beam loadings have demonstrated very good voltage

stability of a few 10^{-4} (for example IBA Rhodotron with beam loading of up to 7:1) during the transients using this technique. Pulse lengths of more than 10 ms can start creating problems of very high energy stored in the power supply in order to be able to deliver the peak power. A 10 ms pulse means a pulsing frequency of 20 Hz. At these levels we enter into the mechanical resonances region of the delicate grid structures of the amplifier tubes. Pulse length of 100 ms and more can create additional issues with electricity grid loading. Main parts of the power supplies should then be dimensioned for the maximal power. This would have an important cost impact. From the pulse structure of the H_2^+ beam and the expected performance of the accelerating cavities, a total peak-power of 2.5 MW during beam extraction, and a 600 kW average power has to be fed to each cavity.

The heavy beam loading induces a large swing of the cavity input impedance. If the cavity is matched (50Ω input impedance) during beam acceleration, the amplifier and transmission line have to deal with an input impedance of about 250Ω when the beam is off. This leads to a Voltage Standing Wave Ratio of $VSWR \approx 5$ and a relative voltage enhancement of about 67% in the transmission line.

Table 9: Comparison of the rf-requirement for the DSRC and achieved performance at PSI

	DSRC	PSI 590 MeV RC	Unit
Operating Frequency	49.2	50.6	MHz
Cavity gap voltage	1	1.4	MV
Average cavity input power	600	700	kW
Maximum amplifier power	2.5 peak	1 cw	MW
Beam loading factor	5.0	1.2	

Since the requirements of the DSRC are close to the achieved performance of the PSI rf-system a possible feeding scheme of the cavities can be extrapolated from the PSI high power amplifier chain. In order to reduce the peak power of the final amplifier stage, two MW-class amplifier chains could be used and coupled to the cavity, as illustrated in Fig. 28. Each cavity will then be equipped with two input power coupler and amplifier chains.

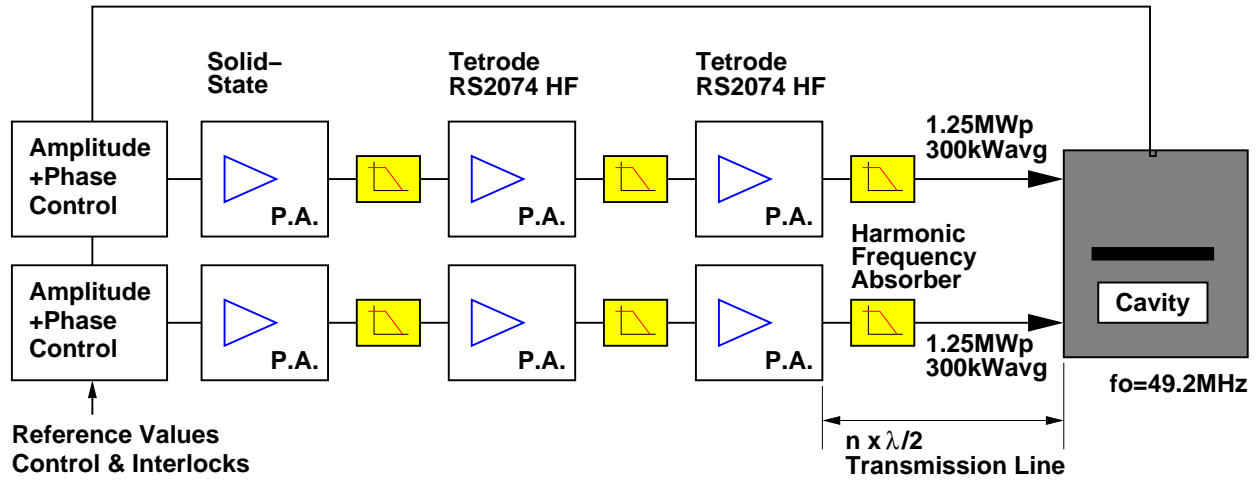


Figure 28: Proposed MW-class amplifier chain

A more modern and powerful power tube for the final amplifier would be the TH525 tetrode, for example. With this tetrode, it might be possible to use one amplifier chain per cavity only. Alternative final amplifier tubes are the 4CM2500KG and 8973 from CPI International.

7. Comments on the scope of this article

The scope of this article has been limited to the systems in the accelerator chain that are critical for the high-intensity design of DAE δ ALUS. These topics are expected to be of wide interest to readers. Several, mostly specialized, topics (subsystems) have not been considered, and we touch on these here briefly.

We have omitted subsystems which are not critical from the point of view of high-intensity operation and which are standard for many operating accelerator facilities. Such systems include beam diagnostics and controls, the beam transfer lines between injector and ring cyclotron, and the transfer line to the beam target.

This article has also not included in-depth discussion of the beam targeting. Development of the target station is an iterative process that accounts for the physics demands for the neutrino flux as well as the operational demands of the high-power beam on the target. The design is underway, inspired by target stations at LANL, ISIS, and PSI. Details of the target station and the neutrino flux will be given in a future article.

However, we point out a few facts about the targeting here. The beam target must accept high average power, but has no special constraints in view of the power density. It is possible to use copper as a material with high thermal conductivity. The beam size can be beam-optically enlarged to obtain a power density that can be safely handled in the copper. PSI operates a MW-class beam dump, made from copper with a conical shape to distribute the beam power in the longitudinal direction. The dump is sectioned into three 0.5 m long segments, to allow a simple exchange of the highly activated segments in case of failure. This dump can serve as a model for higher beam powers. The dimensions can be scaled up to keep the peak temperatures at acceptable levels.

Conventional subsystems are needed. These include the buildings, concrete and steel shielding, electrical installations, radiation monitoring, interlock systems, and venting systems, including monitoring of mobile radioactive isotopes. Practically, the complete electrical power which is used to operate the facility and to generate the intense beam has to be removed from the components by water-cooling circuits. Significant installations will be required for the conventional cooling systems in this high-power accelerator. Finally, specific auxiliary systems are needed for the operation of high-intensity accelerators and targets. Such systems are, for example, shielded exchange flasks for activated components and a hot cell facility for repair work. Much of the design of the conventional subsystems will be site-specific and designed in a later stage of DAE δ ALUS development.

8. Conclusions

In this paper we have addressed some of the most challenging research questions facing the DAE δ ALUS project regarding a cyclotron-based high-power proton driver in the megawatt range with a kinetic energy of 800 MeV. Cyclotrons of this kind would be useful for numerous applications, ranging from particle physics to nuclear waste transmutation.

We identified H₂⁺ as the preferred particle to accelerate, as opposed to bare protons, on the basis of beam dynamics arguments which show that substantially higher beam currents are possible. The area found to be most challenging, and requiring greater research efforts, was the discussion about suppressing H₂⁺ ions with higher-order vibrational states and maintaining the general loss budget at required order of 10⁻⁴ of the total intensity.

Precise beam dynamics simulations with 3D space charge and extraction using a simple H₂⁺ stripping process are the bases for characterization and quantification of the beam halo – one of the most limiting processes in high-power particle accelerators. We show that in the DIC controlled beam losses are well within the allowed margins, and the stripped proton beam from the DSRC can be well matched to the extraction channel.

Initial calculations of vacuum and dissociation cross sections are also within the expectations; however, more dedicated research is needed. For this purpose, a two-phased program is being initiated to optimize source performance and inflection/capture into the DIC. The first phase is an experiment for inflection and

capture into the central region of the DIC; the second is a study of vibrational state distributions in the beam and methods of suppressing the weakly bound states.

The initial design of the rf-system, mostly based on enhanced versions of the PSI cavities, is shown to be feasible for delivering the required rf-power. The required pulse structure (20% duty cycle) is expected to be feasible based on the presented initial calculations.

Achieving the very high proton currents and the required power on target is based on generalized pervance arguments: the space-charge forces at injection energies for the required currents of H_2^+ closely match the conditions in existing high-current proton machines with substantially less beam current. Although the design of the DSRC and the DIC certainly requires further refinement, the design example presented demonstrates the feasibility of achieving the very high performance goals needed for the DAE δ ALUS accelerators.

Acknowledgments

Support for this workshop has been provided through the Majorana Centre from the INFN Eloisatron Project, directed by Prof. Antonino Zichichi. Support for studies is provided by the National Science Foundation and the Massachusetts Institute of Technology. The majority of computations have been performed on the Cray XT4 in the framework of the PSI CSCS “Horizon” collaboration and the local PSI computing resources FELSIM and Merlin4.

References

- [1] M. Larsson, et.al, Dissociative Recombination of H_2^+ studied in CRYRING, *Physica Scripta* 51 (1995) 354–358.
- [2] K. Abrahamsson et.al, CRYRING - a synchrotron, cooler and storage ring, *Nuclear Instruments and Methods in Physics Research B* 79 (1993) 269–272.
- [3] A.S. Schlachter, et al., *Phys Rev A* 27 (1983) 3372.
- [4] T. Suzuki, et al., *Phys Rev A* 50 (1994) 3533.
- [5] T. Azuma, private communication.
- [6] M. D. Williams, K. N. Leung, G. M. Brennen, and D. R. Burns, Testing of a H_2^+ enriched ion source for deuterium simulation, *Rev. Sci. Instrum.* 61, 475 (1990) doi: 10.1063/1.1141278 61 (475).
- [7] Barger V. *et al.*, Report of the US long baseline neutrino experiment study, Tech. rep., arXiv:0705.4396 [hep-ph] (2007).
- [8] L. Calabretta *et al.*, Preliminary Design Study of High-Power H_2^+ Cyclotrons for the DAEDALUS Experiment arXiv: 1107.0652.
- [9] S. Davidson, C. Pena-Garay, N. Rius, A. Santamaria, Present and future bounds on non-standard neutrino interactions, *JHEP.* 2003 (2002) 011. doi:10.1088/1126-6708/2003/03/011.
- [10] The NuTeV collaboration, Zeller G.P. *et al.*, A precise determination of electroweak parameters in neutrino nucleus scattering, *Phys. Rev. Lett.* 88 (2002) 091802.
- [11] M.Seidel, S.Adam, A.Adelmann, C.Baumgarten *et al.*, PRODUCTION OF A 1.3 MW PROTON BEAM AT PSI, in: Proceedings of IPAC 2010, Kyoto, Japan, 2010.
- [12] M.M. Gordon, *Particle Accelerators* 16 (1984) 39–62.
- [13] H. Okuno, *et al.*, *IEEE Trans. Appl. Supercond.* 18 (2008) 226.
- [14] M. Kase, E. Ikezawa, N. Fukunishi, O. Kamigaito, H. Okuno, *et al.*, Present status of the riken ring cyclotron, in: 17th International Conference on Cyclotrons and their Applications, 2004.
- [15] A. Calanna, D. Campo, L. Calabretta, M. Maggiore, L. A. C. Piazza and D. Rifuggiato, A superconducting ring cyclotron to search for cp violation in the neutrino sector, Proceedings of IPAC 2011, San Sebastián, Spain (WEPS072) (2011) 373.
- [16] A. Calanna, L. Calabretta, M. Maggiore, L. A. C. Piazza and D. Rifuggiato, A multi megawatt ring cyclotron to search for CP violation in the neutrino sector, Proceedings of 2011 Particle Accelerator Conference, New York, NY, USA (WEP232) (2011) 1924.
- [17] L. Calabretta, M. Maggiore, L. A. C. Piazza, D. Rifuggiato and A. Calanna, A Multi Megawatt Cyclotron Complex to Search for CP Violation in the Neutrino Sector, 19th International Conference on Cyclotrons and their Applications, Lanzhou, P.R.China and <http://arxiv.org/abs/1010.1493>.
- [18] M. Seidel, *et.al.*, Towards the 2 MW Cyclotron and latest development at PSI, 19th International Conference on Cyclotrons and their Applications, Lanzhou, P.R.China (tum1cio01).
- [19] M. M. Gordon, The Z4 orbit code and the focusing bar fields used in beam extraction calculations for superconducting cyclotrons, *NIM A* 247 (1986) 423–430.
- [20] N. Joshi, M. Droba, O. Meusel and U. Ratzinger, Characterization of volume type ion source for p, H_2^+ and H_3^+ beams, *NIM A* 606 3 (2009) 310–313.
- [21] H. Okuno, private communication (2011).
- [22] H.R. Fitze *et al.*, RF Development at PSI, in: Proc. 17th Int. Conf. on Cyclotrons and their Applications, Tokyo, 2004.
- [23] P.K. Sigg, Cyclotron cavities Part II, cAS2000 (2000).

- [24] M. Maggiore *et al.*, Conceptual design of the RF accelerating cavities for a superconducting cyclotron, Nuclear Instruments and Methods in Physics Research A 557 (2006) 414–420.
- [25] W. Kleevan *et al.*, Recent development and progress of iba cyclotrons, Nuclear Inst. And Methods in Physics Research, B 269 (2011) 2857–2862.
- [26] H.R. Fitze - PSI, private communication (2011).
- [27] H. D. Betz, Rev. of Mod. Phys. 44 (465).
- [28] N E Davison, M J Canty, D A Dohan and A McDonald, Phys Rev C 10 (1974) 50.
- [29] F. Maimone *et al.*, Status of the versatile ion sources (vis), in: Proc. Eur. Part. Acc. Conf., 2008.
- [30] L. Celona *et al.*, Rev. Sci. Instrum. 75 (1423).
- [31] D. Barni, *et al.*, Status of the high current proton accelerator for the trasco program, Tech. rep. (2002).
- [32] I. R. Collins and O. Gröbner and O.B. Malyshev and A. Rossi and P. Strubin and R. Veness, Vacuum stability for ion induced gas desorption, LHC Project Report 312, CERN (1999).
- [33] E. Mahner, Review of heavy-ion induced desorption studies for particle accelerators, PRST-AB 11 (104801).
- [34] M.A. Plum, private communication (2011).
- [35] Y. Bylinski, private communication (2011).
- [36] M.A. Plum *et al.*, SNS stripper foil development program, Nucl. Instrum. Meth. A 590 (2008) 43–47.
- [37] A.O. Lindahl *et al.*, Depletion of the excited state population in negative ions using laser photodetachment in a gas-filled rf-quadrupole ion guide, J. Phys. B: At. Mol. Opt. Phys 43 (115008).
- [38] Y. Liu *et al.*, Beam purification by photodetachment, in: ICIS'11, 2011.
- [39] A. Set *et al.*, Production of low-vibrational-state H_2^+ ions for collision studies, J. Phys. B: At. Mol. Phys 20 (1987) 1509–1515.
- [40] A. Adelman, Loss budget of 200 w inside cyclotron vault established by psi to keep activation levels tolerable for hands-on maintenance, private communication (2011).
- [41] W. McCurdy and R. Haxton, Potential calculations, private communication (2011).
- [42] F. von Busch and G.H. Dunn, Photodissociation of H_2^+ and D_2^+ experiment, Phys Rev A 5 (1972) 1726–1743.
- [43] Proc. Int'l Congress on Advanced Nuclear Power Plants (ICAPP 2002), Accelerator-driven thorium cycle: New technology makes it feasible.
- [44] U.S. Department of Energy, COST/BENEFIT COMPARISON FOR 45 MEV AND 70 MEV CYCLOTRONS, Tech. rep., U.S. Department of Energy - Jupiter <http://www.isotopes.gov/outreach/reports.html> (2005).
- [45] T. Zhang, J. Yang, M. Li, L. Xia, S. An, Z. Yin, J. Zhong, F. Yang, W. Joho, A. Adelman, P. Sigg, Conceptual design of an 800 MeV high power proton driver, Nuclear Instruments and Methods in Physics Research Section B: Beam Interactions with Materials and Atoms 269 (24) (2011) 2964 – 2967. doi:10.1016/j.nimb.2011.04.053. URL <http://www.sciencedirect.com/science/article/pii/S0168583X11004046>
- [46] J. J. Yang, A. Adelman, M. Humbel, M. Seidel, T. J. Zhang, Beam dynamics in high intensity cyclotrons including neighboring bunch effects: Model, implementation, and application, Phys. Rev. ST Accel. Beams 13 (2010) 064201. doi:10.1103/PhysRevSTAB.13.064201. URL <http://link.aps.org/doi/10.1103/PhysRevSTAB.13.064201>
- [47] J.J. Yang, *et al.*, High performance computation on beam dynamics problems in high intensity compact cyclotrons, Sci China Phys Mech Astron 54 S2 (2011) 1–6. doi:10.1007/s11433-011-4544-1.
- [48] Y. J. Bi, A. Adelman, R. Dölling, M. Humbel, W. Joho, M. Seidel, T. J. Zhang, Towards quantitative simulations of high power proton cyclotrons, Phys. Rev. ST Accel. Beams 14 (2011) 054402. doi:10.1103/PhysRevSTAB.14.054402. URL <http://link.aps.org/doi/10.1103/PhysRevSTAB.14.054402>
- [49] A. Adelman, C. Kraus, Y. Ineichen, J. J. Yang, The OPAL (Object Oriented Parallel Accelerator Library) Framework, Tech. Rep. PSI-PR-08-02, Paul Scherrer Institut, http://amas.web.psi.ch/docs/opal/opal_user_guide-1.1.9.pdf (2008-2010).
- [50] APS Neutrino Study, Multi-divisional neutrino study, Tech. rep., American Physical Society (2004). URL <http://www.aps.org/policy/reports/multidivisional/neutrino/>
- [51] Recommendations to the Department of Energy and the National Science Foundation on a Future U.S. Program in Neutrino Oscillations”, submitted by the Neutrino Scientific Assessment Group., Tech. rep. URL http://www.science.doe.gov/hep/hepap_reports.shtm
- [52] Report of the Particle Physics Project Prioritization Panel, Tech. rep. (2008). [link]. URL http://www.er.doe.gov/hep/hepap_reports.shtm
- [53] S. S. C. Law, Neutrino models and leptogenesis, arXiv:0901.1232 [hep-ph].
- [54] C. Amsler *et al.*, Neutrino models and leptogenesis, Physics Letters B 667, see Reviews, chapter 13, “Neutrino Mixing,” by B. Kayser.
- [55] J. Alonso *et al.*, Expression of interest for a novel search for cp violation in the neutrino sector: DAE δ ALUS, arXiv:1006.0260 [physics.ins-det]. URL [arXiv:1006.0260](http://arxiv.org/abs/1006.0260) [physics.ins-det]
- [56] C. Rubbia *et al.*, Conceptual design of a fast neutron operated high power energy amplifier. URL CERN/AT/95-44 (ET)
- [57] N. Fietier, P. Mandrillon, C. Rubbia, A cyclotron-based accelerator for driving the energy amplifier, in: Proc. 14th Intl. Conf. on Cyclotrons and their Applications, Cape Town, 8-13, 1995.
- [58] N. E. A. (NEA), Accelerator-driven systems (ads) and fast reactors (fr) in advanced nuclear fuel cycles, Tech. rep. (2002). URL <http://www.nea.fr/ndd/reports/2002/nea3109-ads.pdf>
- [59] G. Kim, D. May, P. McIntyre, A superconducting isynchronous cyclotron stack as a driver for a thorium-cycle power

- reactor, in: Proc. Intl. Particle Accelerator Conference, Chicago, 2001.
- [60] L. Calabretta, Utilization and reliability of high power proton accelerators, NEA Workshop.
 - [61] L. Calabretta, D. Rifuggiato, M. Maggiore, V. Shchepounov, A superconducting ring cyclotron to deliver high intensity proton beams, in: EPAC 2000, Vienna, Austria, 2000.
 - [62] S. K. Agarwalla, J. M. Conrad, M. Shaevitz, Short-baseline Neutrino Oscillation Waves in Ultra-large Liquid Scintillator Detectors [arXiv:1105.4984](#).
 - [63] A. J. Anderson, J. M. Conrad, E. Figueroa-Feliciano, K. Scholberg, J. Spitz, Coherent Neutrino Scattering in Dark Matter Detectors, *Phys. Rev. D* 84 (2011) 013008. [arXiv:1103.4894](#), [doi:10.1103/PhysRevD.84.013008](#).
 - [64] P. Vogel, J. F. Beacom, The angular distribution of the neutron inverse beta decay, anti- $\nu_e + p \rightarrow e^+ + n$, *Phys. Rev. D* 60 (1999) 053003. [arXiv:hep-ph/9903554](#), [doi:10.1103/PhysRevD.60.053003](#).
 - [65] C. Rubbia, A. Ferrari, Y. Kadi, V. Vlachoudis, Beam cooling with ionization losses, *NIM-A A* 568 (2006) 487.
 - [66] S. Davidson, C. Pena-Garay, N. Rius, A. Santamaria, Present and future bounds on nonstandard neutrino interactions, *JHEP* 0303 (2003) 011. [arXiv:hep-ph/0302093](#).
 - [67] S. A. et.al, Geant4 a simulation toolkit, *NIM-A A* 506 (2003) 250–303.
 - [68] J. A. et.al, Geant4 developments and applications, *IEEE Transactions on Nuclear Science* 53 No. 1 (2006) 270–278.
 - [69] M. Reiser, Theory and design of charged particle beams, Wiley Series in Beam Physics and Accelerator Technology, Wiley-VCH, 2008.
URL <http://books.google.ch/books?id=eegK9Mqgpi4C>
 - [70] G. E. Tripard, W. Joho, Studies on Extraction Efficiency and Energy Spread for the SIN Cyclotron, *Nuclear Instruments and Methods* 79 (1970) 293–303.
 - [71] J. J. Yang, A. Adelman, L. Calabretta, High Intensity Beam Dynamics Simulation for the DAE δ ALUS Cyclotrons, to be published.
 - [72] M. Wurm, et al., The next-generation liquid-scintillator neutrino observatory LENA, *Astropart.Phys.* 35 (2012) 685–732. [arXiv:1104.5620](#).
 - [73] A. Bungau, A. Adelman, J. Alonso, W. Barletta, R. Barlow, et al., An Electron Antineutrino Disappearance Search Using High-Rate ^8Li Production and Decay [arXiv:1205.4419](#).
 - [74] Cyclone-70, Tech. rep., <http://www.iba-cyclotron-solutions.com/products-cyclo/cyclone-70>.
 - [75] Best 70p cyclotron - specifications, Tech. rep., http://www.bestcyclotron.com/product_70p.html.
 - [76] T. Zhang, Z. Li, S. An, Z. Yin, J. Yang, F. Yang, The cyclotron development activities at CIAE, *Nucl. Inst. Meth* 269 (2011) 2863.
 - [77] A. Anderson, J. Conrad, E. Figueroa-Feliciano, C. Ignarra, G. Karagiorgi, et al., Measuring Active-to-Sterile Neutrino Oscillations with Neutral Current Coherent Neutrino-Nucleus Scattering, [arXiv:1201.3805](#).